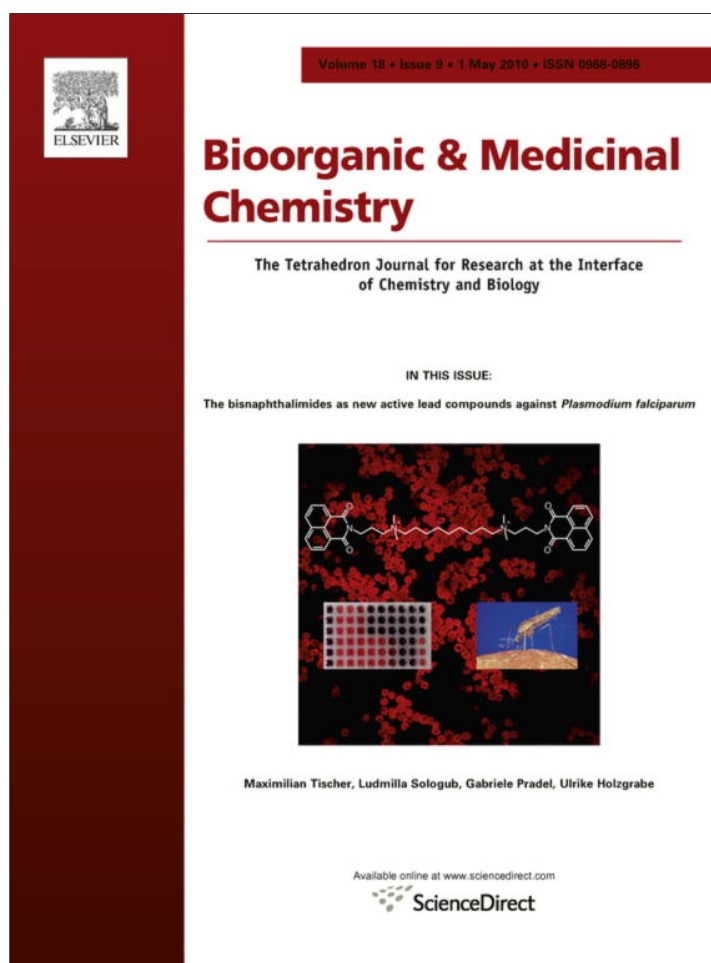


Provided for non-commercial research and education use.
Not for reproduction, distribution or commercial use.



This article appeared in a journal published by Elsevier. The attached copy is furnished to the author for internal non-commercial research and education use, including for instruction at the authors institution and sharing with colleagues.

Other uses, including reproduction and distribution, or selling or licensing copies, or posting to personal, institutional or third party websites are prohibited.

In most cases authors are permitted to post their version of the article (e.g. in Word or Tex form) to their personal website or institutional repository. Authors requiring further information regarding Elsevier's archiving and manuscript policies are encouraged to visit:

<http://www.elsevier.com/copyright>



Contents lists available at ScienceDirect

Bioorganic & Medicinal Chemistry

journal homepage: www.elsevier.com/locate/bmc

Elaborate ligand-based pharmacophore exploration and QSAR analysis guide the synthesis of novel pyridinium-based potent β -secretase inhibitory leads

Afaf Al-Nadaf^a, Ghassan Abu Sheikha^b, Mutasem O. Taha^{c,*}^a Department of Pharmaceutical Chemistry, Applied Science University, Amman, Jordan^b Faculty of Pharmacy Al-Zaytoonah Private University of Jordan, Amman, Jordan^c Drug Discovery Unit, Department of Pharmaceutical Sciences, Faculty of Pharmacy, University of Jordan, Amman, Jordan

ARTICLE INFO

Article history:

Received 22 January 2010

Revised 16 March 2010

Accepted 17 March 2010

Available online 21 March 2010

Keywords:

 β -Secretase inhibitors

Pharmacophore modeling

Ligand-efficiency

Quantitative structure–activity relationship

Receiver-operating characteristic curve

Pyridinium

ABSTRACT

β -Secretase (BACE) inhibitors have potential as anti-Alzheimer's disease treatments prompting us to explore the pharmacophoric space of 129 known BACE inhibitors. QSAR analysis was employed to select optimal combination of pharmacophoric models and 2D physicochemical descriptors capable of explaining bioactivity variation ($r^2 = 0.88$, $F = 60.48$, $r_{LOO}^2 = 0.85$, r_{PRESS}^2 against 25 external test inhibitors = 0.71). We were obliged to use ligand efficiency as the response variable because the logarithmic transformation of bioactivities failed to access self-consistent QSAR models. Three pharmacophoric models emerged in the successful QSAR equation suggesting at least three binding modes accessible to ligands within BACE binding pocket. QSAR equation and pharmacophoric models were validated through ROC curves and were employed to guide synthesis of novel pyridinium-based BACE inhibitors. The best inhibitor illustrated an IC_{50} value of 1.0 μ M against BACE.

© 2010 Elsevier Ltd. All rights reserved.

1. Introduction

Alzheimer's disease (AD) is the most common cause of dementia in older people. The progression of AD involves the destruction of cells that control memory especially in the hippocampus. AD is thought to be caused by the formation of neuritic plaques of aberrantly folded proteins in the brain.¹

Fibrils in neuritic plaques consist mainly of amyloid β -protein ($A\beta$), which is a 40–42 residue-protein generated by cleavage of the extracellular domain of the transmembrane amyloid precursor protein (APP) catalysed by the proteases β - and γ -secretase.²

Familial AD shows several mutations at APP secretase cleavage sites. These seem to affect the pattern of APP processing and lead to increased production of fibril-forming $A\beta$ -peptide.³

It has been shown recently that $A\beta$ -peptide increases with age, particularly in AD patients,^{4,5} prompting significant recent interest in designing potent β - and γ -secretase inhibitors as potential therapeutic agents against AD.^{6,7}

Several classes of β -secretase (BACE) inhibitors were recently reported, including: peptidomimetic inhibitors,⁸ imidazolidinone analogs,⁹ hydroxymethylcarbonyl isosteres,¹⁰ coumarin derivatives,¹¹ flavonoids,¹² cyclic ureas¹³ and acyl guanidines.¹⁴ Furthermore, a recent in silico docking-based screening campaign identified several diverse new micro molar BACE inhibitors.¹⁵

* Corresponding author. Tel.: +962 6 5355000x23305; fax: +962 6 5339649.
E-mail address: mutasem@ju.edu.jo (M.O. Taha).

Clearly, the main focus of recent efforts towards the development of new BACE inhibitors concentrate on structure-based ligand design,^{15,16} with few ligand-based exceptions.^{7,2} To date, several human BACE X-ray complexes are documented in the Protein Data Bank (e.g., PDB codes: 3HVG, 3HW1, 2WEZ, 2WF1, 2WF2, 2WF3, 2WF4, 2NVNN, 2VIE, 2VIJ, 2VIY, 2VIZ, 2VJ6, 2VJ7, 2VJ9 resolution range: 1.60–2.48 Å).^{17–23} However, although considered the most reliable structural information that can be used for drug design, crystallographic structures are limited by inadequate resolution²⁴ and crystallization-related artifacts of the ligand–protein complex.^{25–27} Moreover, crystallographic structures generally ignore structural heterogeneity related to protein anisotropic motion and discrete conformational substrates particularly in cases of pronounced induced-fit protein flexibilities.²⁸

The continued interest in designing new BACE inhibitors, combined with the drawbacks of structure-based design and the significant induced fit flexibility observed for BACE,²⁹ prompted us to explore the possibility of developing ligand-based three-dimensional (3D) pharmacophore(s) integrated within self-consistent QSAR model. This approach avoids the pitfalls of structure-based techniques; furthermore, the pharmacophore model(s) can be used as 3D templates to synthesize new BACE inhibitory scaffolds. We previously reported the use of this innovative approach towards the discovery of new inhibitory leads against glycogen synthase kinase 3β ,³⁰ hormone sensitive lipase,³¹ bacterial MurF,³² protein tyrosine phosphatase 1B³³ and influenza neuraminidase.³⁴

We employed the HYPOGEN module from the CATALYST software package³⁵ to construct numerous reasonable binding hypotheses for BACE inhibitors. Subsequently, genetic function algorithm (GFA) and multiple linear regression (MLR) analyses were employed to search for an optimal QSAR that combine high-quality binding pharmacophores with other molecular descriptors and capable of explaining bioactivity variation across a collection of diverse BACE inhibitors. The optimal pharmacophores were further validated by evaluating their abilities to successfully classify a list of compounds as actives or inactives by assessing their receiver-operating characteristic (ROC) curves. The optimal pharmacophores were employed as guides to synthesize new series of active BACE inhibitors. The synthesized compounds illustrated low micro molar potencies.

CATALYST models drug–receptor interaction using information derived only from the drug structure.^{35–43} HYPOGEN identifies a 3D array of a maximum of five chemical features common to active training molecules, which provides a relative alignment for each input molecule consistent with their binding to a proposed common receptor site. The chemical features considered can be hydrogen bond donors and acceptors (HBD and HBA), aliphatic and aromatic hydrophobes (Hbic), positive and negative ionizable (Poslon and Neglon) groups and aromatic planes (RingArom). The conformational flexibility of training ligands is modeled by creating multiple conformers, judiciously prepared to emphasize representative coverage over a specified energy range. CATALYST pharmacophores have been used as 3D queries for database searching and in 3D-QSAR studies.^{44–46,32,47,33}

2. Results and discussion

CATALYST enables automatic pharmacophore construction by using a collection of molecules with activities ranging over a number of orders of magnitude. CATALYST pharmacophores (hypotheses) explain the variability of bioactivity with respect to the geometric localization of the chemical features present in the molecules used to build it. Different hypotheses were generated for a series of BACE inhibitors. A total of 129 compounds were used in this study (Fig. 1 and Table A in Supplementary data). Six training subsets were selected from the collection (Table 1). Each subset consisted of inhibitors of wide structural diversity. The biological activity in the training subsets spanned from 3.5 to 4.0 orders of magnitude. Genetic algorithm and multiple linear regression statistical analysis were subsequently employed to select an optimal combination of complementary pharmacophores capable of explaining bioactivity variations among all inhibitors.

2.1. Data mining and conformational coverage

The literature was surveyed to collect as many structurally diverse BACE inhibitors as possible (1–129, see Table A in Supplementary data and Fig. 1).^{15,48} Although the collected compounds are quite diverse and hence not expected assume similar binding modes or bind to the same set of binding pockets, the combination of pharmacophore modeling and QSAR analysis should allow access to all possible binding modes assumed by different inhibitors within the enzyme. In this approach we employ large list of diverse inhibitors to generate large number of potential binding hypotheses (240 pharmacophores in this case). Subsequently, the resulting pharmacophores are allowed to compete within the context of QSAR analysis. Pharmacophore models that emerge within the optimal QSAR model(s) (i.e., capable of explaining bioactivity variation across all collected compounds) should cover all binding modes of diverse training molecules. We previously reported the use of this innovative approach towards unveiling diverse ligand-

binding modes within glycogen synthase kinase 3 β ,³⁰ hormone sensitive lipase,³¹ bacterial MurF,³² protein tyrosine phosphatase 1B,³³ influenza neuraminidase,³⁴ estrogen receptor β ligands.⁷⁶

The collected inhibitors were carefully selected in such a way that they were all bioassayed employing identical assay procedures and conditions to allow proper QSAR modelling. The 2D structures of the inhibitors were imported into CATALYST and converted automatically into plausible 3D single conformer representations. The resulting 3D structures were used as starting points for conformational analysis and in the determination of various molecular descriptors for QSAR modeling.

The conformational space of each inhibitor was extensively sampled utilizing the poling algorithm employed within the CONFIRM module of CATALYST⁴⁹ and via the 'Best' module to ensure extensive sampling of conformational space. Efficient conformational coverage guarantees minimum conformation-related noise during pharmacophore generation and validation stages.⁴⁹

2.2. Exploration of BACE pharmacophoric space

CATALYST-HYPOGEN enables automatic pharmacophore construction by using a collection of at least 16 molecules with bioactivities spanning over 3.5 orders of magnitude.^{35,39–43} Accordingly, the fact that we have an informative list of 129 BACE inhibitors of evenly spread bioactivities over more than 3.5 orders of magnitude prompted us to employ HYPOGEN algorithm to identify as many pharmacophoric binding modes assumed by diverse BACE inhibitors as possible.

HYPOGEN implements an optimization algorithm that evaluates large number of potential binding models for a particular target through fine perturbations to hypotheses that survived the constructive and subtractive phases of the modeling algorithm (see Section 4.1.4).³⁹ The number of evaluated pharmacophoric models is reflected by the configuration (Config.) cost calculated for each modeling run. It is generally recommended that the Config. cost of any HYPOGEN run not to exceed 17 (corresponding to 2¹⁷ hypotheses to be assessed by CATALYST) to guarantee thorough analysis of all models.⁴⁰

The size of the investigated pharmacophoric space is a function of training compounds, selected input chemical features and other CATALYST control parameters.⁴⁹ Restricting the extent of explored pharmacophoric space should improve the efficiency of optimization via allowing effective evaluation of limited number of pharmacophoric models. On the other hand, extensive restrictions imposed on the pharmacophoric space might reduce the possibility of discovering optimal pharmacophoric hypotheses, as they might occur outside the 'boundaries' of the pharmacophoric space.

Therefore, we decided to explore the pharmacophoric space of BACE inhibitors within plausible 'boundaries' through 24 HYPOGEN automatic runs and employing six carefully selected training subsets (i.e., from the collected compounds): subsets A, B, C, D, E, and F in Table 1. The training compounds in these subsets were selected in such away to guarantee maximal 3D diversity and continuous bioactivity spread over more than 3.5 logarithmic cycles. Furthermore, the training inhibitors were selected in such a way that differences in their anti-BACE bioactivities are primarily attributable to the presence or absence of pharmacophoric features (e.g., HBA or HBD or Hbic or RingArom) rather than steric shielding and/or bioactivity-enhancing or -reducing auxiliary groups (e.g., electron donating or withdrawing groups). We gave special emphasis to the 3D diversity of the most-active compounds in each training subset (Table 1) because of their significant influence on the extent of the evaluated pharmacophoric space during the constructive phase of HYPOGEN algorithm (see Section 4.1.4).

Guided by our reasonably restricted pharmacophoric exploration concept, we instructed HYPOGEN to explore only 4- and 5-featured

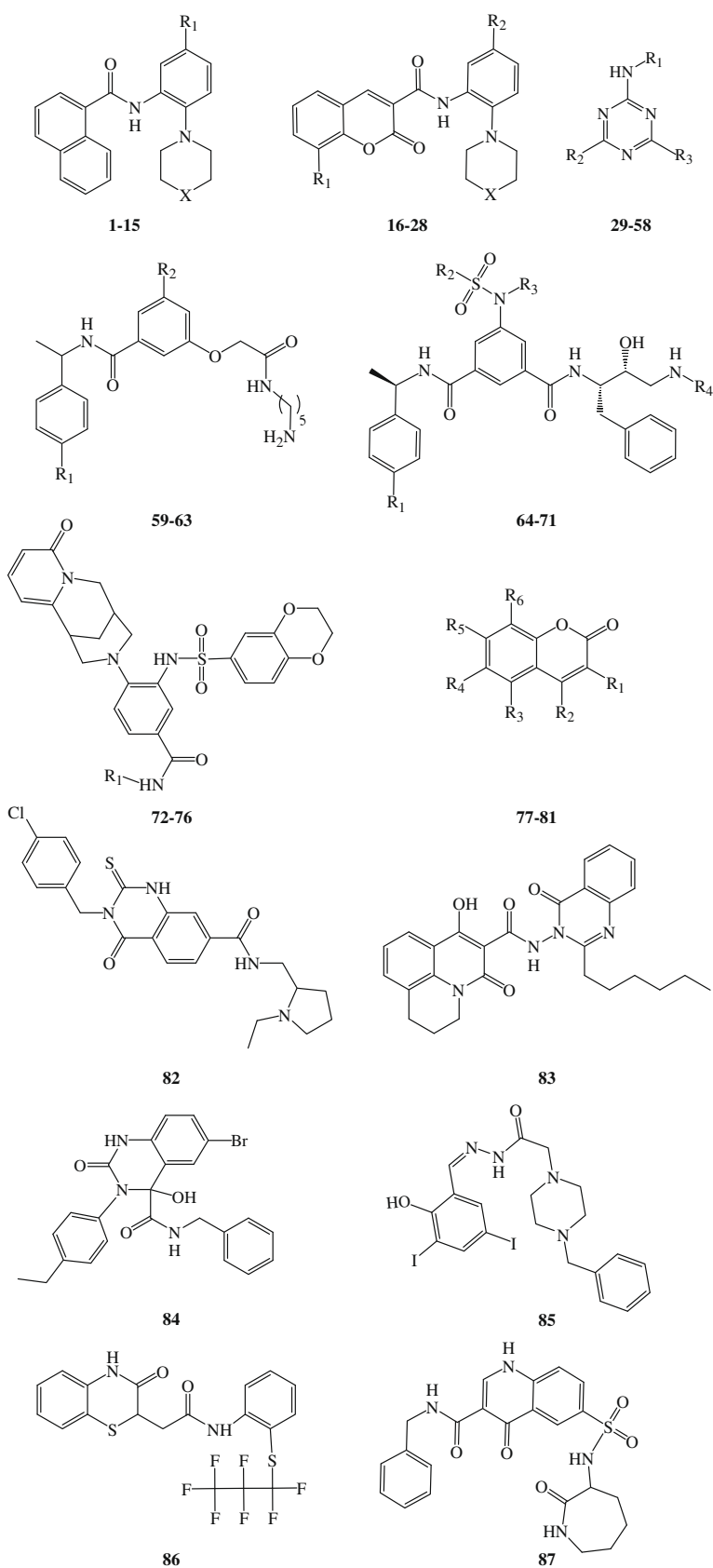


Figure 1. The chemical scaffolds of training compounds, the corresponding structures and bioactivities are as in Table A in Supplementary data.

pharmacophores, that is, ignore models of lesser number of features (as shown in Table B in Supplementary data). The later restriction

has the advantage of narrowing the investigated pharmacophoric space and representing the feature-rich nature of BACE ligands.

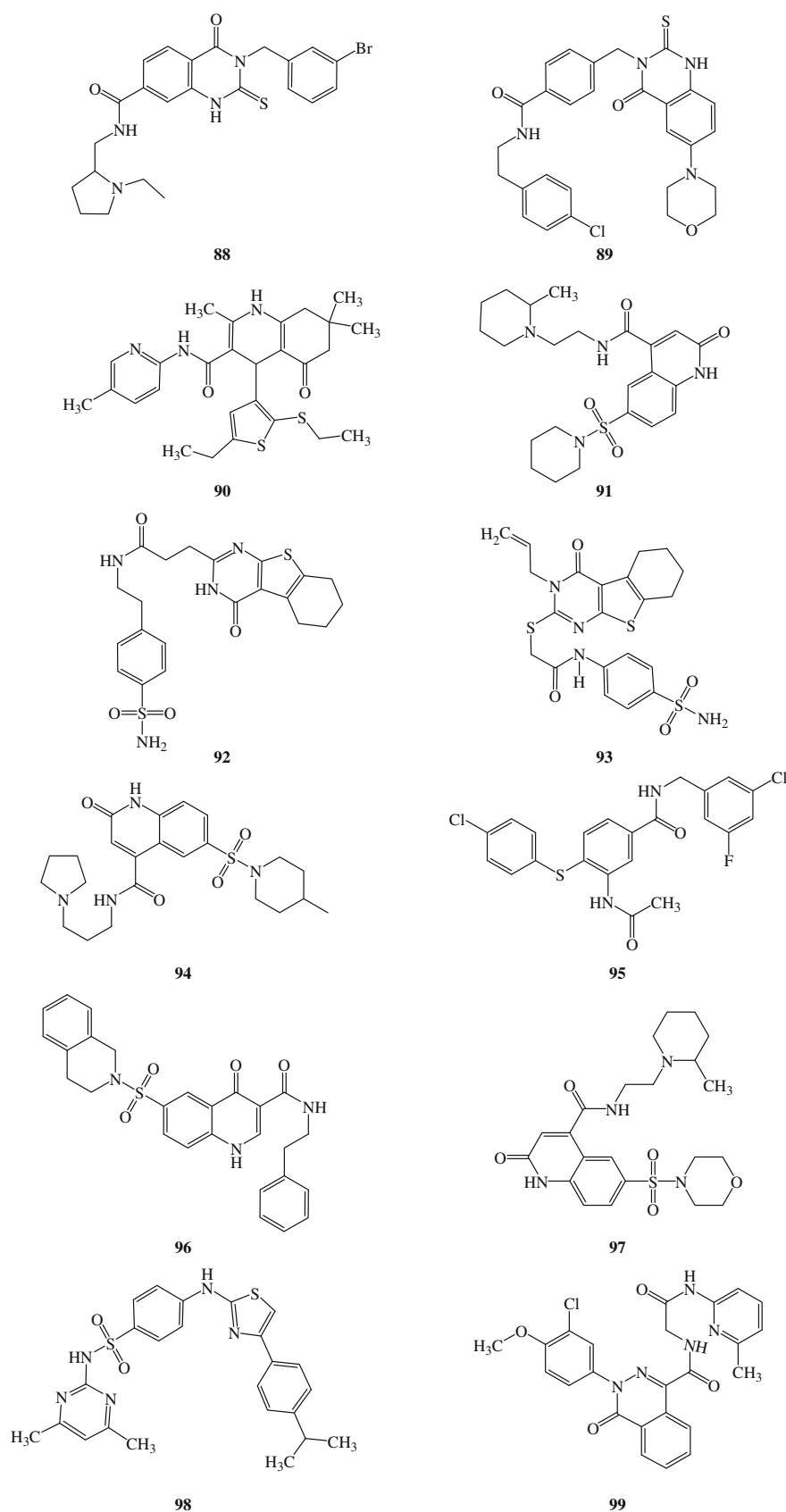


Figure 1 (continued)

In each run, the resulting binding hypotheses were automatically ranked according to their corresponding 'total cost' value, which is

defined as the sum of error cost, weight cost and configuration cost (see Section 4.1.5 for details about pharmacophore validation).^{35,39–43}

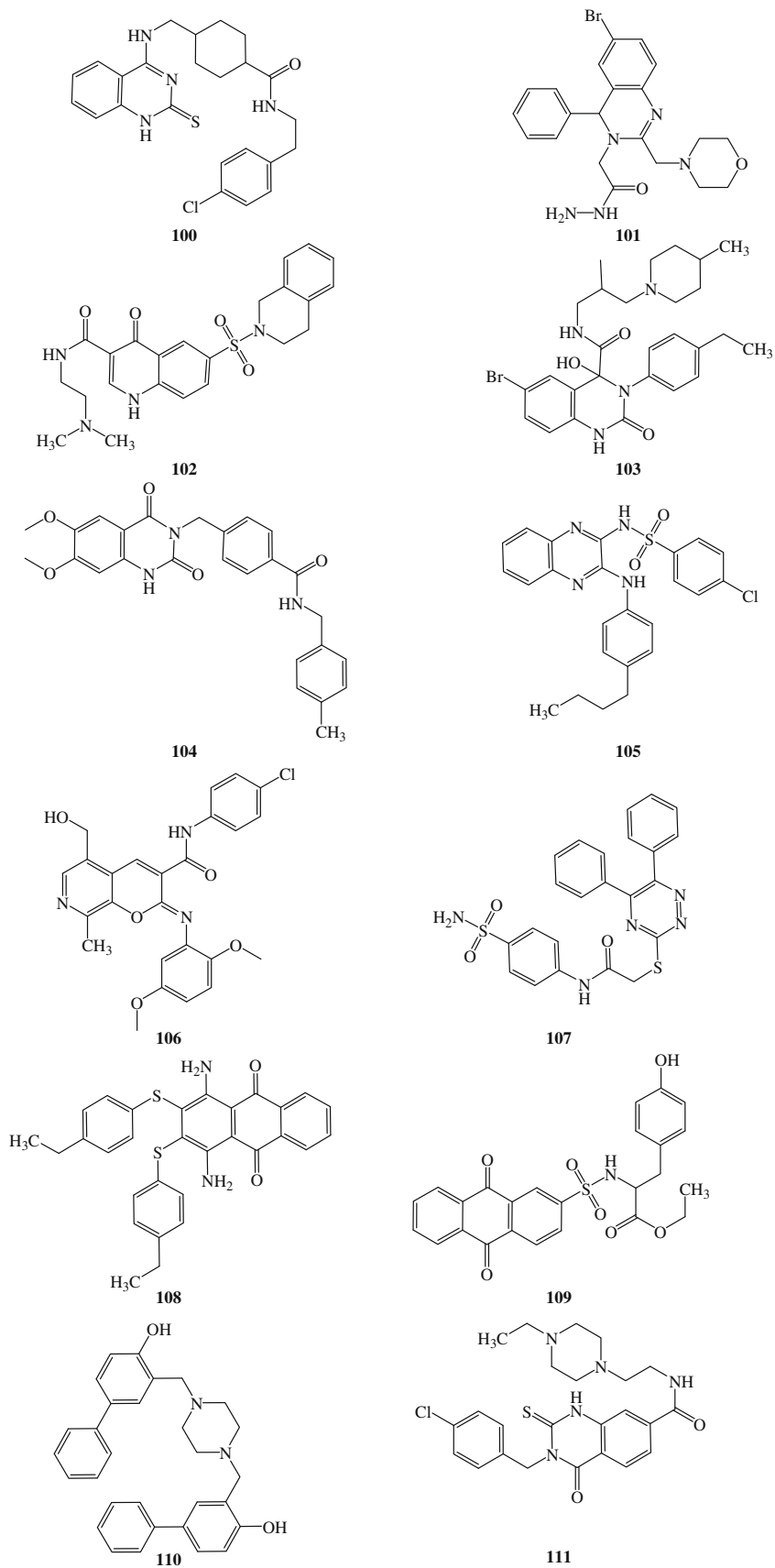


Figure 1 (continued)

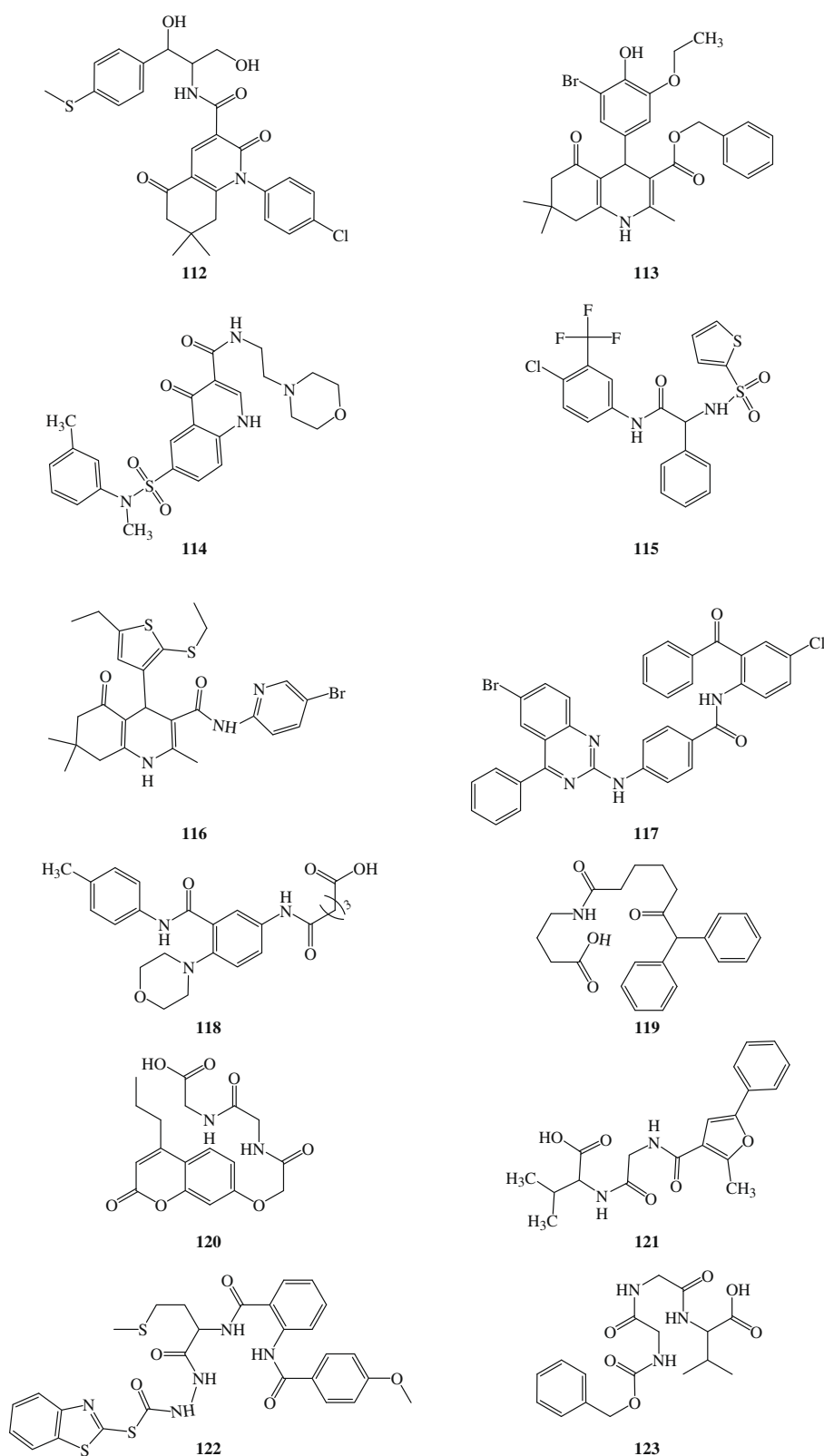


Figure 1 (continued)

Eventually, 240 pharmacophore models emerged from 24 automatic HYPOGEN runs, out of which only 226 models illustrated confidence levels $\geq 85\%$ (Fisher scrambling criteria, see Section 4.1.5).^{35,39–43} These successful models were clustered and their best representatives (45 models, see Section 4.1.6) were used in subse-

quent QSAR modeling. Table C in Supplementary data shows the statistical criteria of the best representatives, which shared comparable features and acceptable statistical success criteria.

Emergence of several statistically comparable pharmacophore models suggests the ability of BACE ligands to assume multiple

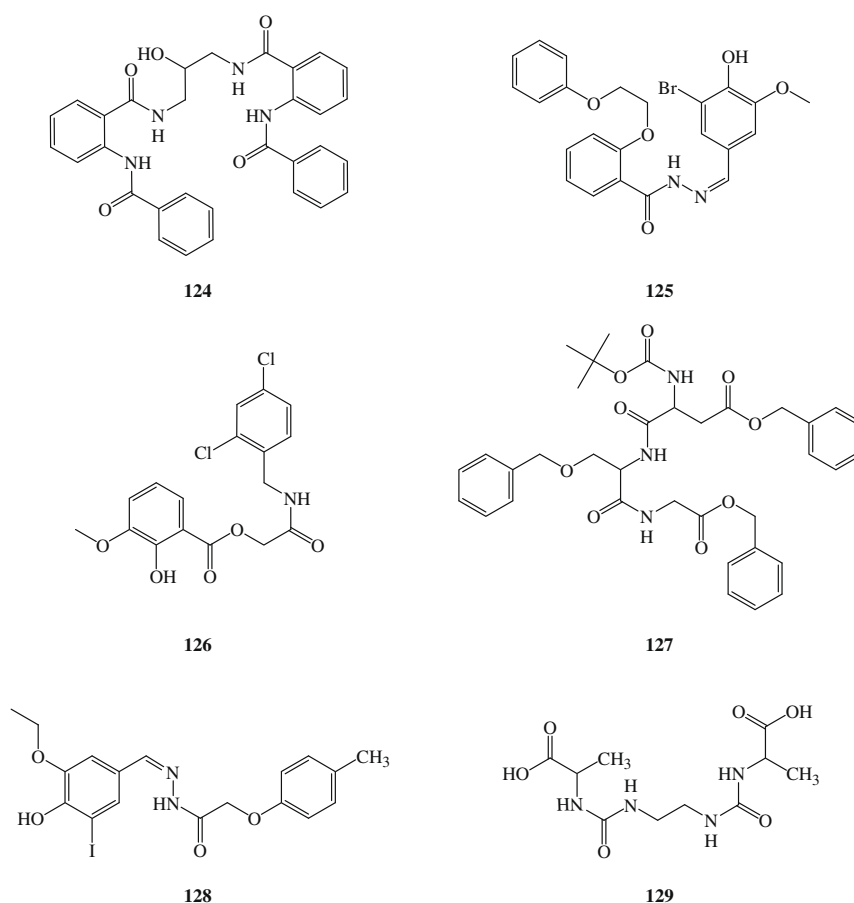


Figure 1 (continued)

Table 1
Training subsets employed in exploring the pharmacophoric space of BACE inhibitors, numbers correspond to compounds in Table A in Supplementary data and Figure 1

Training sets	Most active ^a	Moderate active	Least active ^b
A	5, 7, 9, 11, 13	1, 2, 4, 6, 16, 32, 33, 38, 56	53, 58, 98
B	5, 8, 20, 27, 28	18, 31, 32, 33, 61, 63, 65, 67, 69, 70, 71	108, 125, 126
C	5, 8, 20, 27, 28	31, 32, 61, 63, 65, 69, 67, 70, 71	108, 125, 126
D	7, 8, 14, 19, 27, 28	31, 33, 35, 45, 61, 63, 85, 110	123, 129
E	5, 8, 9, 20, 28	17, 18, 26, 38, 39, 41, 45, 60, 63	125, 126
F	7, 8, 13, 14, 27	1, 3, 17, 26, 30, 31, 43, 53, 55, 56	119, 126, 123

^a Potency categories as defined by Eqs. 2 and 3.

^b Potency categories as defined by Eqs. 2 and 3.

pharmacophoric binding modes within the binding pocket. Therefore, it is quite challenging to select any particular pharmacophore hypothesis as a sole representative of the binding process.

2.3. QSAR modeling

The predictive value of pharmacophore hypotheses as 3D-QSAR models is usually limited by steric shielding and bioactivity-enhancing or reducing auxiliary groups.⁴² This point combined with the fact that pharmacophore modeling of BACE inhibitors furnished numerous binding hypotheses of comparable success criteria (Table C in Supplementary data) prompted us to employ classical QSAR analysis to search for the best combination of pharmacophore (s) and other 2D descriptors capable of explaining bioactivity variation across the whole list of collected inhibitors (1–129, Table A in Supplementary data and Fig. 1). We employed genetic function approximation and multiple linear regression

QSAR (GFA-MLR-QSAR) analysis to search for optimal QSAR equation (s).³⁵

Fit values obtained by mapping the 45 representative hypotheses against collected BACE inhibitors (1–129) were enrolled together with a selection of 2D descriptors as independent variables GFA-MLR-QSAR analysis (see Section 4.1.7).^{51,52} Unfortunately, all our attempts to achieve self-consistent and predictive QSAR models were futile prompting us to evaluate an alternative modeling strategy, namely, to employ ligand efficiency [$\log(\text{IC}_{50})/\text{MW}$] as the response variable instead of activity [$\log(\text{IC}_{50})$]. The fact that many training compounds exhibited similar potencies despite their wide structural variations (e.g., 61 training compounds illustrated IC_{50} values of 100 μM) prompted us to maximize bioactivity variance through division (normalization) over molecular weights. This novel strategy proved successful in achieving self-consistent QSAR models.

To access the predictive power of the resulting QSAR models on an external set of inhibitors, we randomly selected 25 molecules

(marked with asterisks in Table A in Supplementary data) and employed them as external testing set for validating the QSAR models. Moreover, all QSAR models were cross-validated automatically using the leave-one-out cross-validation in CERIUS2.^{50,51}

Eq. 1 shows the details of the optimal QSAR model. Figure 2 shows the corresponding scatter plots of experimental versus estimated bioactivities for the training and testing inhibitors:

$$\begin{aligned} \frac{\text{Log}(1/\text{IC}_{50})}{\text{MW}} = & 7.9 \times 10^{-5} \text{Hypo1/21} + 3.0 \times 10^{-4} \text{Hypo6/18} \\ & + 1.5 \times 10^{-4} \text{Hypo10/10} - 4.7 \times 10^{-5} \text{JursDPSA3} \\ & - 1.4 \times 10^{-4} \text{Log } P + 9.0 \times 10^{-4} \text{AtypeC3} \\ & + 3.6 \times 10^{-4} \text{SdsCH} - 4.7 \times 10^{-4} \chi^0 \\ & + 1.1 \times 10^{-3} \chi^2 + 4.5 \times 10^{-3} \text{ShadowXZfrac} \\ & - 5.1 \times 10^{-4} \text{LUMO} - 3.1 \times 10^{-3} r_{104}^2 = 0.88, \\ F = & 60.48, n = 104, r_{\text{BS}}^2 = 0.89, r_{\text{LOO}}^2 = 0.85, \\ r_{\text{PRESS}}^2 = & 0.71 \end{aligned} \quad (1)$$

where, r_{104} is the correlation coefficient against 104 training compounds, r_{LOO}^2 is the leave-one-out correlation coefficient, r_{BS}^2 is the bootstrapping regression coefficient and r_{PRESS}^2 is the predictive r^2

determined for 25 test compounds.^{50,51} Hypo10/10, Hypo6/18 and Hypo1/21 represent the fit values of the training compounds (as calculated from Eq. 5) against the 10th, 6th and 1st pharmacophore models in 10th, 18th and 21st automatic runs, respectively, as arranged in Tables B and C under Supplementary data. JursDPSA3 is the difference in atomic charge-weighted surface areas calculated by subtracting atomic charge-weighted positive solvent-accessible surface area minus atomic charge-weighted negative solvent-accessible surface area. Log P is the logarithmic transformation of the oil/water partition coefficient. AtypeC3 is atom-type-based Alog P descriptor related to the hydrophobic contribution of carbon atoms in a particular molecule. SdsCH is the electro-topological state index of $-\text{CH}=\text{}$ atoms. χ^0 and χ^2 are the zero and 2nd order molecular connectivity indices. ShadowXZfrac is a Shadow descriptor related to the area of molecular shadow in the XZ plane calculated by aligning the molecules according to their principal moments of inertia in the X, Y and Z axes. LUMO is the energy of the lowest unoccupied molecular orbital calculated by semiempirical quantum mechanical method (MOPAC).^{45,46,32,51,53}

Emergence of three pharmacophoric models in Eq. 1 suggests the existence of at least three binding modes assumed by inhibitors within the binding pocket of BACE. Figures 3 and 6 show Hypo10/10; Hypo6/18 and Hypo1/21 and how they map training

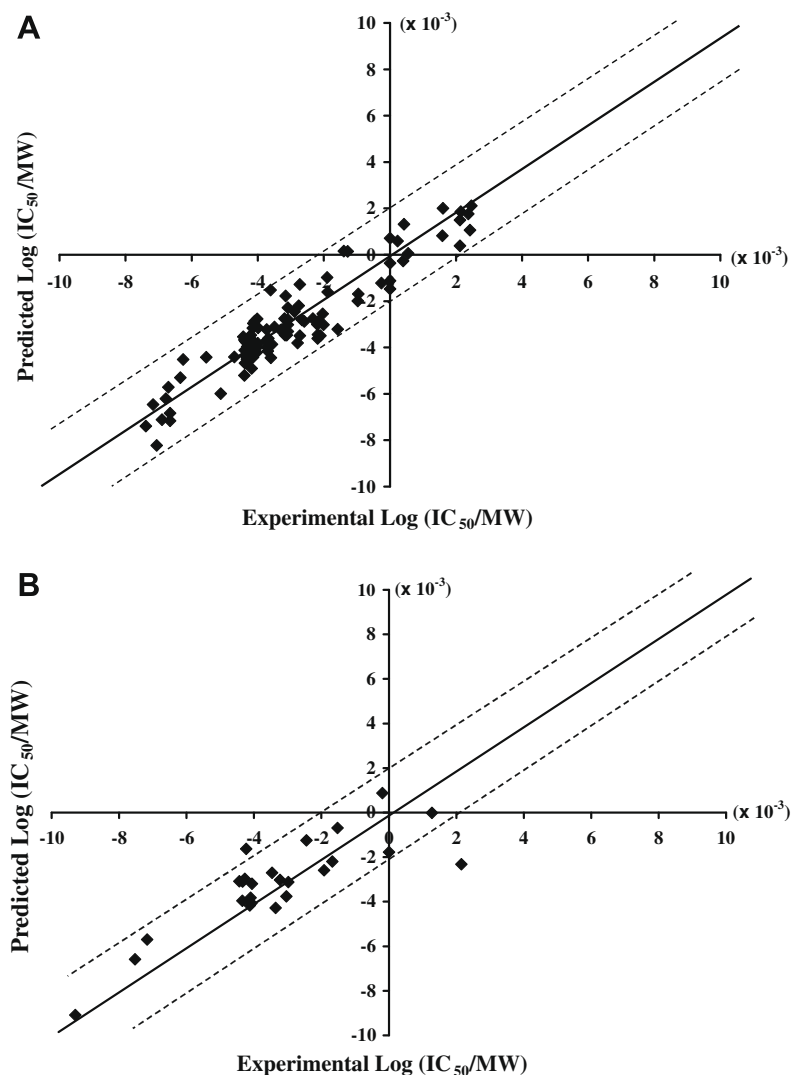


Figure 2. Experimental versus fitted (A, 105 compounds, $r_{\text{LOO}}^2 = 0.85$) and predicted (B, 25 compounds, $r_{\text{PRESS}}^2 = 0.71$) bioactivities calculated from the best QSAR model (Eq. 1). The solid lines are the regression lines for the fitted and predicted bioactivities of training and test compounds, respectively, whereas the dotted lines indicate the $\pm 2 \times 10^{-3}$ log(IC_{50})/MW error margins.

compound **13** ($IC_{50} = 0.046 \mu M$) and some synthesized compounds, while Table 2 shows the X, Y, and Z coordinates of the three pharmacophores.

Emergence of electrotopological, Shadow and connectivity descriptors in Eq. 1 illustrate certain role played by the ligands' topology in the binding process. However, despite their predictive significance, their information content is quite obscure. Emergence of a hydrophilicity-related descriptor, that is, JursDPSA3, combined with two hydrophobicity-related descriptors, that is, log *P* and AtypeC3, all in association with negative regression coefficients suggests that optimal ligand/BACE affinity requires certain optimal hydrophilic/hydrophobic balance.

Finally, emergence of LUMO in Eq. 1 combined with a negative slope suggests that ligand/BACE affinity favors electrophilic ligands probably due to π -stacking with certain electron-rich aromatic centers in the binding pocket.

2.4. Receiver operating characteristic (ROC) curve analysis

To further validate the resulting models (both QSARs and pharmacophores), QSAR-selected pharmacophores were subjected to receiver-operating curve (ROC) analysis. In ROC analysis, the ability of a particular pharmacophore model to correctly classify a list of compounds as actives or inactive is indicated by the area under the curve (AUC) of the corresponding ROC as well as other parameters: overall accuracy, overall specificity, overall true positive rate and overall false negative rate (see Section 4.1.8 for more details). Table 3 and Figure 4 show the ROC performances of our QSAR-selected pharmacophores.

Clearly from Table 3 and Figure 4 that Hypo10/10 and Hypo6/18 significantly outperformed Hypo1/21, which is probably attributed to the absence of a positive ionizable feature from Hypo1/21 compared to Hypo10/10 and Hypo6/18.

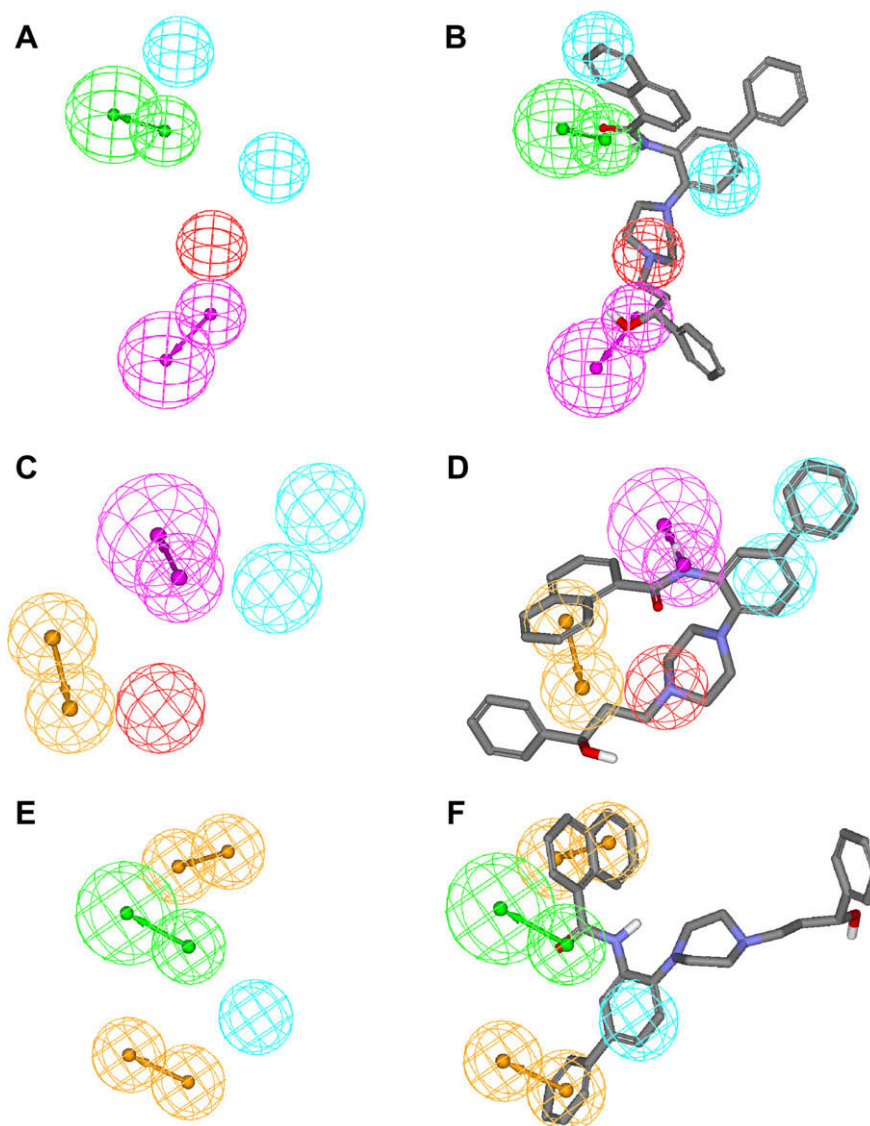


Figure 3. Pharmacophoric features of QSAR-selected binding models. Light blue spheres represent Hbic features, red spheres represent Poslon features, green-vectored spheres encode for HBAs, violet vectored spheres encode HBDs, and RingArom as orange vectored spheres. (A) Hypo10/10, (B) Hypo10/10 fitted against **13** (Table A in Supplementary data and Figure 1, Fit value = 9.9, $IC_{50} = 0.046 \mu M$), (C) Hypo6/18, (D) Hypo6/18, fitted against **13** (Fit value = 9.6), (E) Hypo1/21, and (F) Hypo1/21 fitted against **13** (Fit value = 10.3).

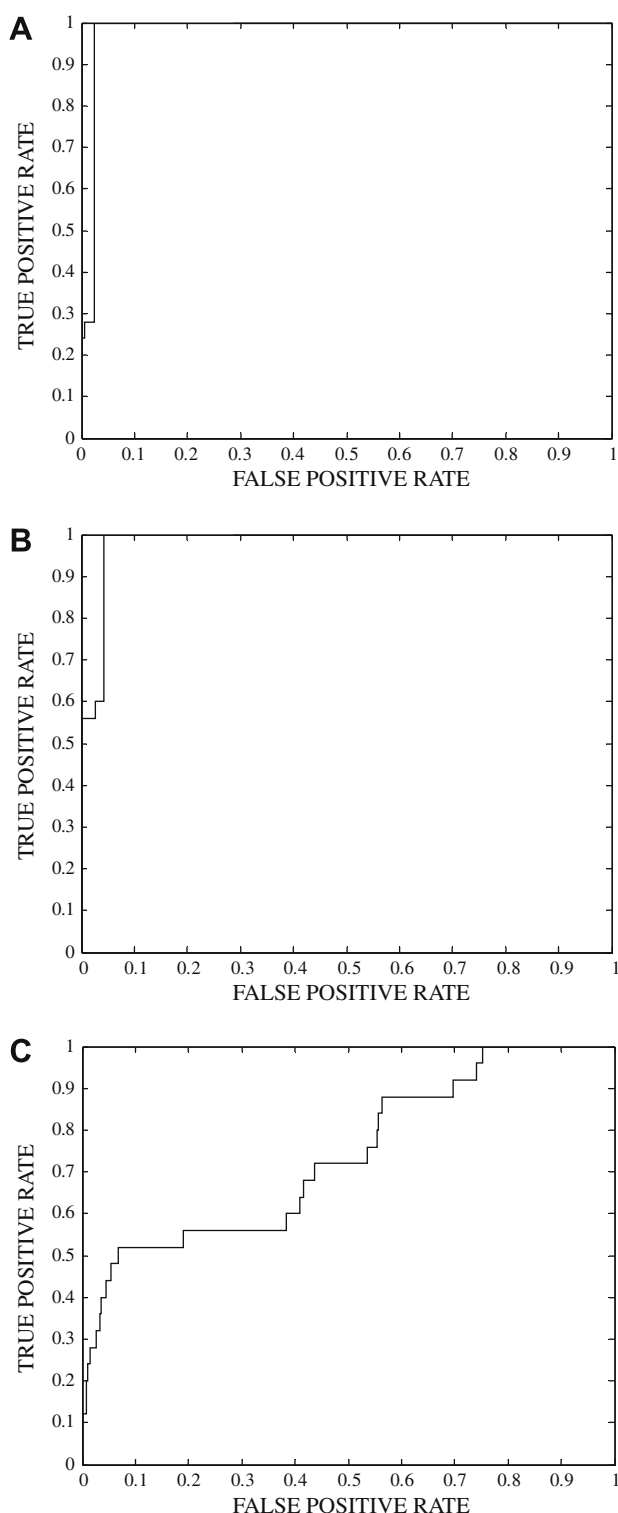


Figure 4. Receiver operating characteristic (ROC) curves of QSAR-selected pharmacophores: (A) Hypo10/10, (B) Hypo6/18 and (C) Hypo1/21.

2.5. Comparing pharmacophore models with crystallographic complexes

To further emphasize the validity of our pharmacophore/QSAR modeling approach, we compared the crystallographic structures of two BACE/ligand complexes⁷⁷ (PDB codes: 2ISO and 2IRZ) with Hypo10/10 and Hypo6/18. Figure 5 shows the chemical structures

of the ligands and compares their BACE complexes with the ways they map Hypo10/10 and Hypo6/18 employing rigid mapping, that is, fitting the ligands' bound states against corresponding pharmacophores without conformational adjustments.

Fitting the hydroxyethyl amine fragment of 2ISO ligand against HBA and Poslon features in Hypo10/10 (Fig. 5b) corresponds to hydrogen-bonding and electrostatic interactions connecting this fragment with the hydroxy and carboxylate side chains of SER35, ASP32 and ASP228, respectively, as in Figure 5c. Similarly, mapping the ligand's amidic carbonyl with a HBA feature in Hypo10/10 corresponds to hydrogen-bonding interaction connecting this carbonyl with the hydroxyl side chain of THR232 (Fig. 5b and c). Finally, fitting the fluorobenzene and benzylic groups of 2ISO ligand against two Hbic features in Hypo10/10 (Fig. 5b) correlates with stacking the fluorobenzene and benzylic rings against the aromatic side chains of TYR14, PHE108 and TRP115, respectively, as in Figure 5c.

Similarly, fitting the benzylic amino of 2IRZ ligand against Poslon feature in Hypo6/18 (Fig. 5e) corresponds to electrostatic attraction connecting this group with the carboxylate side chains of ASP32 and ASP228 (Fig. 5f), while mapping the amidic NH of the ligand against HBD feature in Hypo6/18 (Fig. 5e) agrees with hydrogen bonding connecting this group with the peptidic carbonyl of GLY230 (Fig. 5f). On the other hand, mapping the fluorobenzene of 2IRZ ligand against two Hbic features in Hypo6/18 (Fig. 5e) seems to correspond to hydrophobic interactions tying this fragment with the hydrophobic side chains of ALA335 and LEU30, as in Fig. 5f. Finally, the central *meta* trisubstituted benzene ring of 2IRZ ligand is shown in Figure 5e to have less-than-optimal mapping against a central RingArom feature in Hypo6/18, which seems to correlate with aromatic ring stacking against the adjacent co-planar amide side chain of GLN73.

Clearly from the above discussion, Hypo10/10 and Hypo6/18 represent two valid binding modes assumed by ligands within BACE. Furthermore, these models point to limited number of critical interactions required for high ligand-BACE affinity in each of the binding modes. In contrast, crystallographic complexes reveal many bonding interactions without highlighting critical ones. Incidentally, Figure 5c and f only show interactions corresponding to pharmacophoric features while other binding interactions were hidden for clarity.

2.6. Synthesis and bioactivities of pharmacophore-guided novel BACE inhibitors

The fact that pharmacophores Hypo10/10 and Hypo6/18 were significantly superior to Hypo1/21 vis-à-vis their ROC performances and QSAR slopes, prompted us to employ the former models as templates for building novel BACE inhibitors. We envisaged that a terminal pyridinium moiety should correspond to the positive ionizable features in both pharmacophores, furthermore, the pyridinium ring should provide wide electrophilic surface of pronounced negative LUMO energy to satisfy the requirements of QSAR Eq. 1.

Incidentally, although positively-charged, and therefore unable to cross the blood-brain barrier, pyridinium-based drugs can be devised in the form of uncharged 1,4-dihydro-pyridine surrogate prodrugs capable of crossing the blood-brain-barrier and get oxidized to pyridinium salts in the brain.^{70,71}

The spatial arrangement of pharmacophoric features in both models confined us to *meta*-disubstituted benzene as linker scaffolds in our proposed compounds. Moreover, we proposed mono-substituted aromatic amide on the other side of the molecules to correspond with the terminal hydrophobic features in Hypo10/10 and Hypo6/18 (Figs. 3 and 7). We evaluated several electronically diverse substituents at this side, namely, unsubstituted benzene, *m*-methyl, *p*-methyl, *p*-chloro, and *p*-methoxy groups.

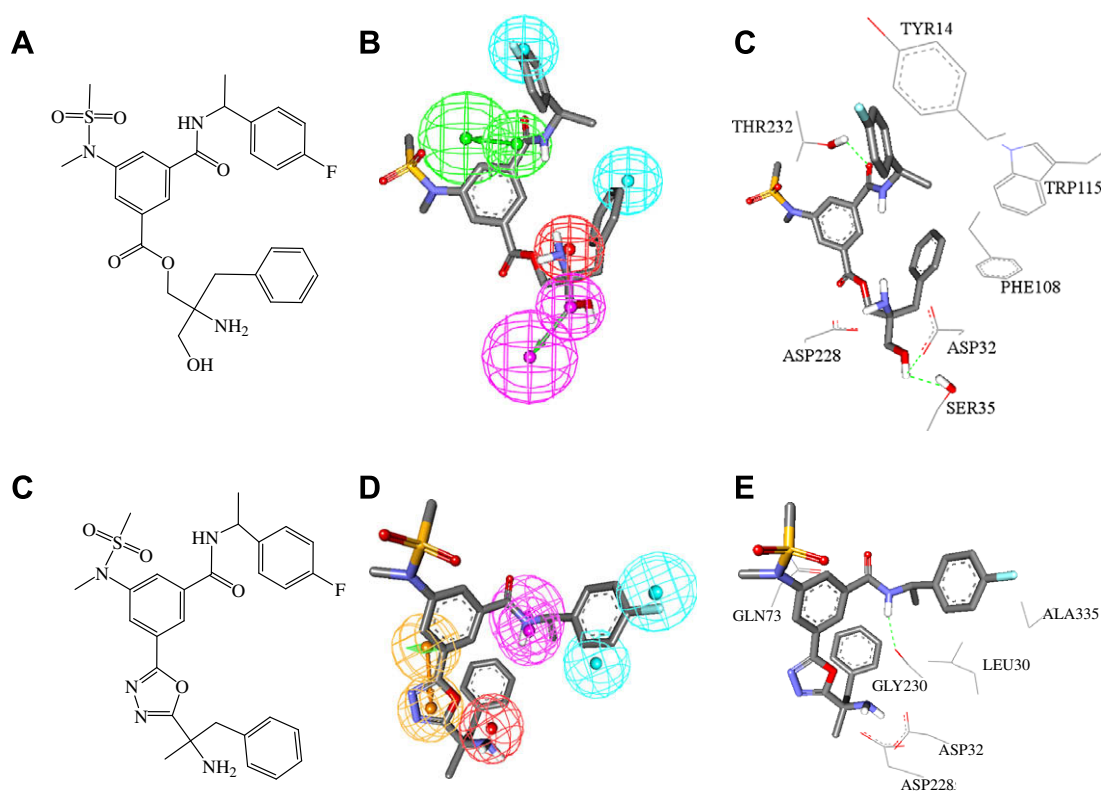


Figure 5. Co-crystallized ligands of BACE X-ray structures 2ISO (resolution = 2.20 Å) and 2IRZ (resolution = 1.80 Å).⁷⁷ (A) and (D) the chemical structures of the co-crystallized ligands of 2ISO and 2IRZ, respectively, (B) and (E) mapping Hypo10/10 and Hypo6/18 against the co-crystallized ligands of 2ISO and 2IRZ (rigid mapping), respectively, (C) and (F) binding pockets of 2ISO and 2IRZ, respectively, complexed with their corresponding co-crystallized ligands.

Accordingly, we explored the structure-activity profiles of 22 novel structures constructed based on *m*-aminobenzoic acid or *m*-diaminobenzene scaffolds, as shown in Table 4.

Synthesis commenced by forming the *N*-phenyl-*m*-nitrobenzamide, *N*-(*m*-nitrophenyl)-benzamide and *N*-(*m*-nitrophenyl)-benz-sulfonamide derivatives (Schemes 1–3). Subsequent reduction of the nitro groups with either sodium dithionite⁶³ or stannous dichloride^{64,65} offered the corresponding aromatic amines (Schemes 4 and 5) that were acylated with mono-chloroacetyl chloride (Scheme 6). Finally, fusion of the resulting chloroacetylated derivatives with pyridine, nicotinamide or *N*-phenylethyl nicotinamide offered the targeted pyridinium derivatives (Scheme 7).

The synthesized compounds were bioassayed employing fluorescent resonance energy transfer (FRET)-based assay.⁶⁸ The bioassay procedure was validated several times employing several concentrations of the standard BACE inhibitor Lys-Thr-Glu-Glu-Ile-Ser-Glu-Val-Asn-Statine-Val-Ala-Glu-Phe.⁷⁵

Although nicotinamide-based pyridinium derivatives (**171–178**, Table 4) successfully fitted all 3 pharmacophore models, as clearly evident from Figure 7a and Table 4, we were prompted to evaluate simpler unsubstituted pyridinium derivatives (**164–170**, Table 4) to assess the significance of the *meta*-amide substituents (in nicotinamide analogues **171–178**) on anti-BACE bioactivity. These derivatives successfully fit Hypo6/18 and Hypo1/21 and miss a hydrogen-bond donor feature in Hypo10/10.

Clearly from Table 4, our proposed compounds were predicted to have moderate anti-BACE bioactivities (low micromolar) compared to the nanomolar potencies of some training compounds (e.g., **13**, **11**, **12**, **5**, **14**, and **9**, Fig. 1 and Table A in Supplementary data). Still, the fact that pyridinium rings possess LUMO values outside the corresponding range of training compounds (Tables D and E in Supplementary data) cast doubt on the ability of our QSAR equation to accurately predict the bioactivities of

the proposed compounds,⁷⁴ and therefore, provided us with further impetus to explore the anti-BACE bioactivities of this novel class. Tables D and E in the Supplementary data show the different descriptor values of collected and synthesized anti-BACE compounds.

Surprisingly, bioassay results show that nicotinamide analogues (**171–178**) exhibited generally similar or inferior anti-BACE profiles compared to their unsubstituted pyridinium analogues, as seen in Table 4. We believe this odd conduct is related to hydration-promoting effects produced by the nicotinamide amidic moieties, which seems to offset their bioactivity gains from fitting the hydrogen-bond donor feature in Hypo10/10 (Fig. 7a). This point combined with the observation that sulfonamide derivatives (**170**, **177**, **178**, and **185**) exhibited generally inferior anti-BACE bioactivities compared to their amide analogues (**167**, **174**, **176** and **184**, respectively), which seem also to be explainable by the profound hydration of their sulfonamide linkers, prompted us to tether hydrophobic phenylethyl side chains to the nicotinamide moieties in **179–185** to attempt counterbalance hydration. Extensive ligand hydration can compete, and therefore, hinder ligand-receptor binding.

Addition of the phenylethyl fragment enhanced the bioactivity of **184** (% inhibition at 50 μ M = 100%, IC₅₀ = 2.2 μ M) compared to unsubstituted analogue **169** (% inhibition at 50 μ M = 68%, IC₅₀ = 13.0 μ M) and the nicotinamide analogue **176** (% inhibition at 50 μ M = 24%). A similar trend is seen with **185** (% inhibition at 50 μ M = 36%) compared to the nicotinamide analogue **178** (% inhibition at 50 μ M = 3.6%). Phenylethyl side chain-related bioactivity improvements in these cases can also be attributed to extra interactions in the binding site unexplained by the pharmacophore model and mediated by the phenylethyl side chain (i.e., extra to their proposed hydration-counterbalance effect mentioned earlier). In fact, docking studies suggest the existence of mutual

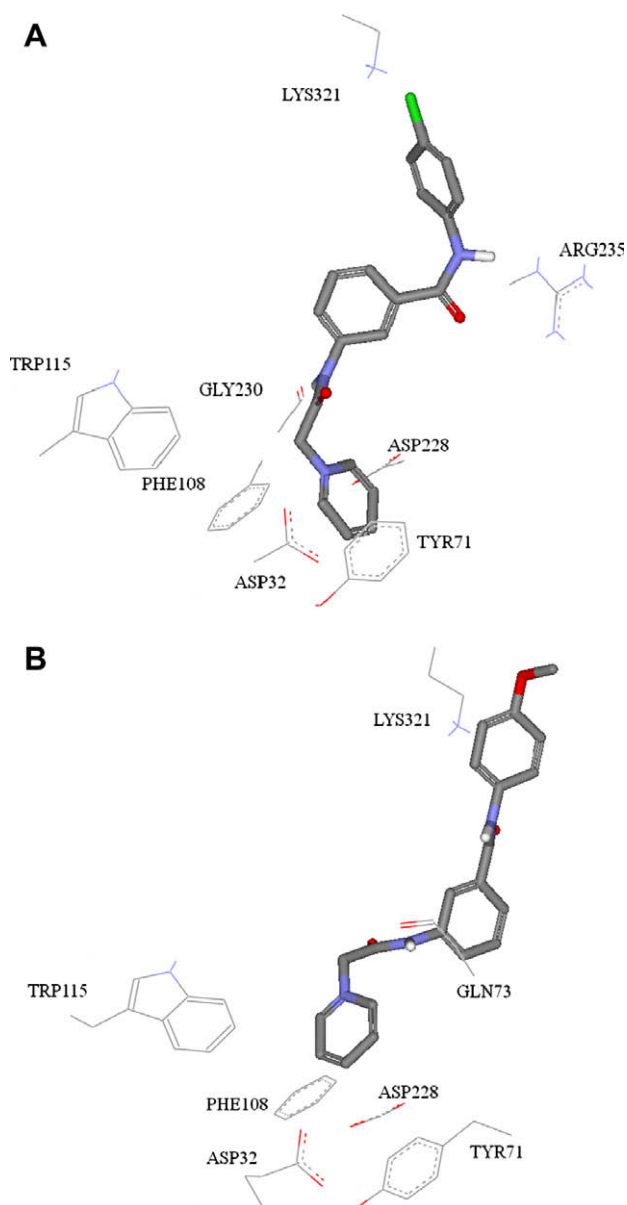


Figure 6. Optimal docked poses of compounds **166** and **167**.

π -stacking interactions between the phenolic side chain of TYR71 and the phenylethyl side chain (see discussion below, Fig. 6b).

Still, in cases of chloro and methoxy derivatives **181** (% inhibition at 50 μ M = 78%, IC_{50} = 12.0 μ M) and **182** (% inhibition at 50 μ M = 44%), respectively, addition of phenylethyl fragments significantly reduced their anti-BACE bioactivities compared to their unsubstituted counterparts **166** (% inhibition at 50 μ M = 100%, IC_{50} = 1.0 μ M) and **167** (% inhibition at 50 μ M = 100%, IC_{50} = 3.7 μ M), respectively, and their nicotinamide analogues **173** (% inhibition at 50 μ M = 64%, IC_{50} = 30.2 μ M) and **174** (% inhibition at 50 μ M = 100%, IC_{50} = 1.9 μ M). We believe this conduct is because **166** and **167** assume different, and more stable, binding poses from those predicted by our pharmacophore hypotheses. Figure 6 shows two optimal binding poses of the two compounds produced employing LIGANDFIT docking engine via default docking settings.⁶⁹ Clearly from the figure the pyridinium moieties of **166** and **167** dip in an electron-rich aromatic/anionic pocket composed of TRP115, PHE108, ASP32, ASP228 and TYR71, while the middle amidic NHs of **166** and **167** are hydrogen-bonded to GLY230 and

GLN73, respectively. On the other hand, the electron-rich methoxybenzene aromatic ring and chloro terminals of **166** and **167** are involved in charge-transfer complex and electrostatic attraction, respectively, with the quaternary ammonium of LYS321. These later interactions are not represented in CATALYST pharmacophoric features, which explain the failure of our models in predicting these binding modes and the excellent potencies of **166** and **167**. The nicotinamide and phenylethyl nicotinamide substituents in the corresponding analogues **173**, **174**, **181** and **182** seem to shift the chloro and methoxybenzene away from the quaternary ammonium of LYS321 and therefore disrupt interactions with LYS321 leading to reduction in anti-BACE bioactivity.

It remains to be mentioned that we validated the selectivity of our potent derivatives against a closely-related aspartic protease: renin. Table 5 shows the inhibitory profiles of **166**, **167**, **169**, **174**, **179**, **181** and **184** against renin. Clearly, the compounds showed minimal inhibitory profiles against renin albeit with increasing trend upon association with phenylethyl side chains.

2.7. Comparison of QSAR-selected pharmacophores with docking into BACE binding site

Pharmacophore features obtained by pharmacophore/QSAR modeling can be compared with the structure of BACE binding site to identify probable residues important for ligand binding and inhibition. Therefore, some of our potent synthesized compounds were fitted against our QSAR-selected pharmacophores, and the resulting mapped conformers were compared with docked poses of these compounds into BACE binding site (PDB code: 2IRZ, resolution 1.8 Å). The docking experiments were performed employing LIGANDFIT docking engine and through default docking parameters.⁶⁹ However, we confined the docking simulation to rigid (or semi-rigid) docking of pharmacophore-fitted conformers to avoid unnecessary exploration of irrelevant docked conformers, which should focus the attention on probable binding residues corresponding to features within our QSAR-selected pharmacophores.

The features in Hypo10/10 as well as the alignment of **184** (IC_{50} = 2.2 μ M) as proposed by Hypo10/10 were compared with the way this compound docks into the binding pocket of BACE, as in Figure 7a and b. A marked similarity was observed between the features proposed by the pharmacophore model and the ligand binding features in the docked structure.

In one of the high-ranking docked poses of **184** (Fig. 7b) the pyridinium group was placed at close proximity to the carboxylate of ASP228 in the binding pocket. This interaction corresponds to a Poslon feature in Hypo10/10 mapping the pyridinium group of **184**. Similarly, the docking experiment suggests that the nicotinamide NH in **184**, interacts with amidic carbonyl of GLY230, which seems to agree with mapping this group with a HBD feature in Hypo10/10 (Fig. 7a). The central *meta*-diaminobenzene ring of **184** is docked adjacent to the aliphatic side chain of THR72, which correspond nicely to mapping this group against a central Hbic feature in Hypo10/10. Finally, mapping the terminal tolyl amide moiety of **184** with HBA and Hbic features in Hypo10/10 corresponds with hydrogen bonding and hydrophobic interactions with the side chains of LYS321, LEU267 and VAL309, respectively (Fig. 7a and b).

Comparably, the docked pose of **174** (IC_{50} = 1.9 μ M) corresponds to fitting **174** against binding model Hypo6/18 (Fig. 7c and d). The pyridinium moiety of **174** apparently electrostatically interacts with the carboxylates of ASP228 and ASP32, which corresponds to mapping this moiety with the Poslon feature in Hypo6/18. Similarly, the central *m*-aminobenzamide linker of **174** is directed by the docking engine towards the indole of TRP115 suggesting significant mutual π -stacking, as in Figure 7d. This agrees with mapping the *m*-aminobenzamide of **174** onto a RingArom feature

Table 2
Pharmacophoric features and corresponding weights, tolerances and 3D coordinates of Hypo10/10, Hypo 6/18 and Hypo 1/21

Model	Definitions	Chemical features							
		HBA		HBD		Hbic	Hbic	Poslon	
Hypo10/10 ^a	Weights	2.30497		2.30497		2.3049	2.30497	2.30497	
	Tolerances	1.60	2.20	1.60	2.20	1.60	1.60	1.60	
	Coordinates	X	1.47	1.09	-4.28	-6.60	-0.64	6.81	-2.59
		Y	-2.04	-3.83	4.23	4.63	-3.18	0.07	0.96
Z	-2.63	-5.01	0.11	-1.74	2.42	-2.23	-0.10		
Hypo 6/18 ^b		HBD		Hbic	Hbic	Poslon	RingArom		
	Weights	2.11185		2.1118	2.11185	2.11185	2.11185		
	Tolerances	1.60	2.20	1.60	1.60	1.60	1.60	1.60	
	Coordinates	X	-0.02	-0.43	2.03	5.70	-3.79	-4.53	-6.06
Y		3.24	3.32	0.30	2.17	0.35	5.17	2.61	
Z		-1.05	-4.02	-1.04	-0.39	0.30	-0.22	0.09	
Hypo 1/21 ^c		HBA		Hbic	RingArom		RingArom		
	Weights	2.59597		2.59597	2.59597	2.59597			
	Tolerances	1.60	2.20	1.60	1.60	1.60	1.60	1.60	
	Coordinates	X	4.61	5.75	3.80	7.97	8.92	1.78	4.36
Y		-1.86	-4.49	2.22	2.82	0.55	-4.35	-5.10	
Z		1.20	2.20	1.54	1.27	2.97	-1.90	-3.23	

^a Hypo10/10: the 10th pharmacophore hypothesis generated in the 10th HYPOGEN run (as in Tables B and C in Supplementary data).

^b Hypo6/18: the 6th pharmacophore hypothesis generated in the 18th HYPOGEN run (as in Tables B and C in Supplementary data).

^c Hypo 1/21: the 1st pharmacophore hypothesis generated in the 21st HYPOGEN run (as in Tables B and C in Supplementary data).

Table 3
ROC^a performances of QSAR-selected pharmacophores as 3D search queries

Pharmacophore model	ROC ^a -AUC ^b	ACC ^c	SPC ^d	TPR ^e	FNR ^f
Hypo10/10	0.982	0.961	0.988	0.28	0.011345
Hypo6/18	0.981	0.961	0.975	0.60	0.024311
Hypo1/21	0.738	0.961	0.9611	0.96	0.038898

^a ROC: receiver operating characteristic.

^b AUC: area under the curve.

^c ACC: overall accuracy.

^d SPC: overall specificity.

^e TPR: overall true positive rate.

^f FNR: overall false negative rate.

in Hypo6/18. The amidic NH of the terminal *p*-anisidine of **174** seem to hydrogen-bond with the side chain of THR232 in the docked pose, which agrees with mapping the same NH by a HBD feature in model Hypo6/18. Similarly, mapping the methoxybenzene terminal of **174** with two Hbic features correlates with hydrophobic interactions tying this group with the side chain linkers of SER325 and ARG235.

Similarly, the docked pose of **169** approximate its mapped pose against Hypo1/21: The toloylamide ring of **169** is placed by the docking engine at close proximity to the aromatic rings of TYR71, PHE108, and TRP115 (Fig. 7f) suggesting the existence of mutual aromatic π -stacking interactions and apparently corresponding to mapping the toloylamide with Hbic feature in Hypo1/21 (Fig. 7e). Furthermore, LigandFit directed the central *m*-diaminobenzene **169** towards ILE110 suggesting mutual hydrophobic interactions, which agrees with fitting this group against a Hbic feature in Hypo1/21. Similarly, mapping the acetamido carbonyl of **169** against a HBA feature in Hypo1/21 corresponds to a hydrogen-bonding interaction tying this group with the hydroxyl of THR231 (Fig. 7e and f). Finally, the docking engine directed the terminal pyridinium moiety of **169** perpendicular to the amidic side chain of ASN233 suggesting the existence of mutual π -stacking interactions and corresponding to a RingArom feature in Hypo1/21 mapping this pyridinium moiety.

3. Conclusion

BACE inhibitors are currently considered as potential treatments for AD. The pharmacophoric space of BACE inhibitors was

explored via six diverse sets of inhibitors and using CATALYST-HYPOGEN to identify high quality binding model(s). Subsequently, genetic algorithm and multiple linear regression analysis were employed to access optimal QSAR model capable of explaining anti-BACE bioactivity variation across 129 collected BACE inhibitors ($r_{104}^2 = 0.879$, $F = 60.48$, $n = 104$, $r_{BS}^2 = 0.001$, $r_{LOO}^2 = 0.846$, r_{PRESS}^2 against 25 external test inhibitors = 0.705). Three pharmacophoric models emerged in the QSAR equation suggesting the existence of at least three distinct binding modes accessible to ligands within BACE binding pocket. The QSAR equation and the associated pharmacophoric models were used to guide synthetic exploration of a new series of BACE inhibitors that resulted in several novel low micro-molar BACE inhibitors.

4. Experimental

4.1. Molecular modeling

4.1.1. Software and hardware

The following software packages were utilized in the present research:

- CATALYST (Version 4.11), Accelrys Inc. (www.accelrys.com), USA.
- CERIU2 (Version 4.10), Accelrys Inc. (www.accelrys.com), USA.
- CS ChemDraw Ultra 6.0, Cambridge Soft Corp. (<http://www.cambridgesoft.com>), USA.
- Pharmacophore and QSAR modeling studies were performed using CATALYST (HYPOGEN module) and CERIU2 software suites from Accelrys Inc. (San Diego, California, www.accelrys.com) installed on a Silicon Graphics Octane2 desktop workstation equipped with a dual 600 MHz MIPS R14000 processor (1.0 GB RAM) running the Irix 6.5 operating system. Structure drawing was performed employing ChemDraw Ultra 6.0 which was installed on a Pentium 4 PC.

4.1.2. Data set

The structures of 129 BACE-1 inhibitors (Table A in Supplementary data) were collected from published literature.^{15,48} All collected inhibitors were assayed employing identical assay procedures and conditions in order to allow proper QSAR correlation. The in vitro bioactivities of the collected inhibitors were expressed

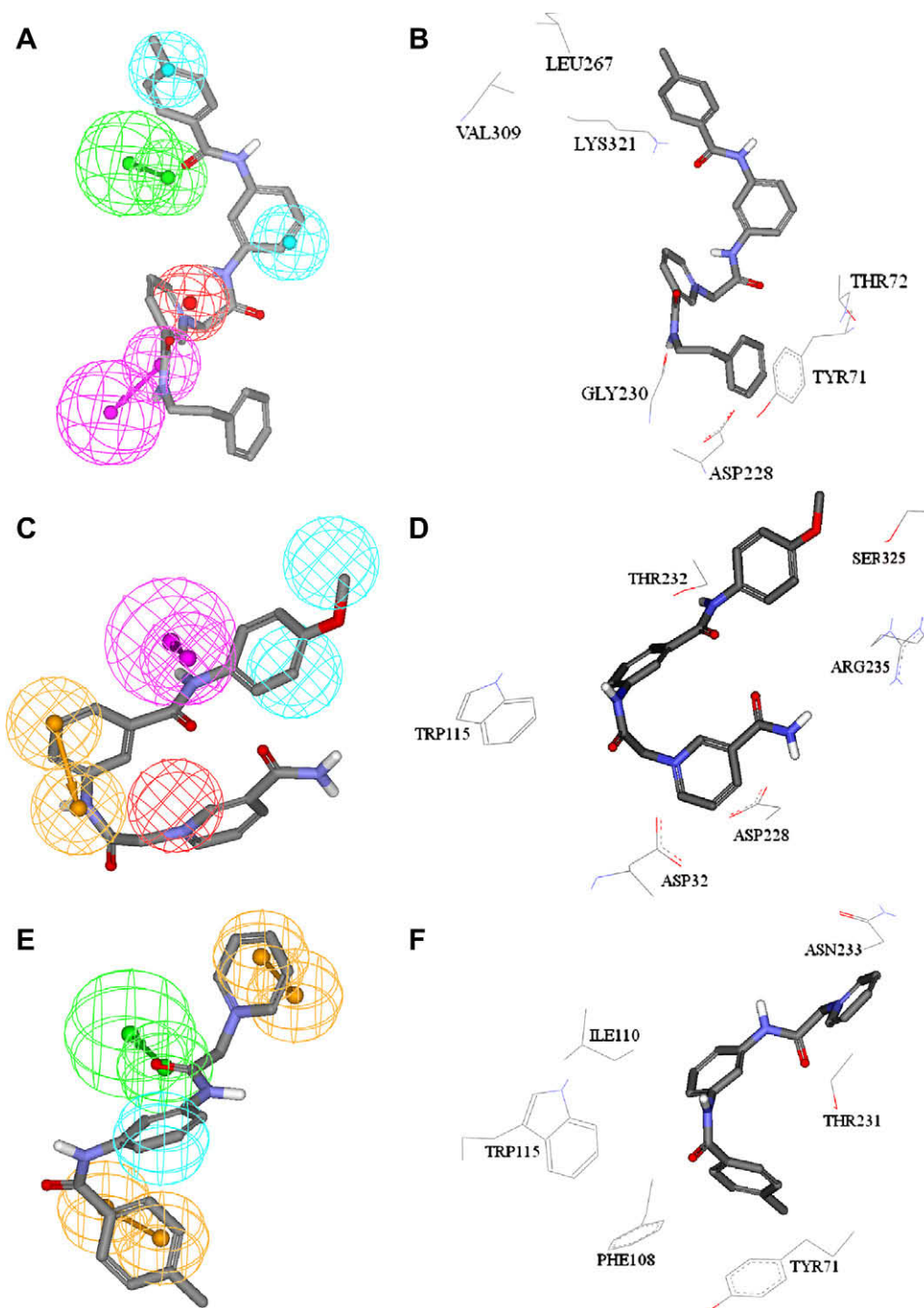


Figure 7. (A), (C) and (E) Show mapping of Hypo10/10, Hypo6/18 and Hypo1/21 against the synthesized compounds **184** ($IC_{50} = 2.2 \mu M$), **174** ($IC_{50} = 1.9 \mu M$), and **169** ($IC_{50} = 13 \mu M$) (Table 4), respectively, while (B), (D) and (F) illustrate corresponding docked poses of the same compounds in BACE (PDB code: 2IRZ, resolution = 1.8 Å).

as the concentration of the test compound that inhibited the activity of BACE-1 by 50% (IC_{50}). Table A in Supplementary data shows the structures and IC_{50} values of the considered inhibitors. The logarithm of measured IC_{50} (μM) values were used in pharmacophore modeling and QSAR analysis, thus correlating the data linear to the free energy change.

In cases where IC_{50} is expressed as being higher than $100 \mu M$ (e.g., **74**, **100**, **101**, **107**, **112** and **117**), it was assumed it equals $100 \mu M$. In cases where IC_{50} is expressed as being higher than $500 \mu M$ (e.g., **118**, **120**, **122**, **125** and **129**), it was assumed it equals

$500 \mu M$. (Table A in Supplementary data, Fig. 1). These assumptions are necessary to allow statistical correlation and QSAR analysis. The logarithmic transformation of IC_{50} values should minimize any potential errors resulting from this assumption.

The two-dimensional (2D) chemical structures of the inhibitors were sketched using ChemDraw Ultra, installed on a PC, and saved in MDL-mol file format. Subsequently, they were imported into CATALYST, converted into corresponding standard 3D structures and energy minimized to the closest local minimum using the molecular mechanics CHARMM force field implemented in CATALYST. The

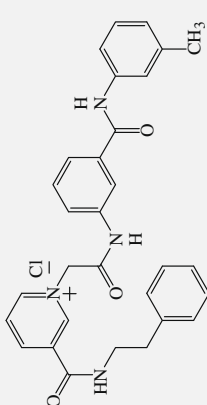
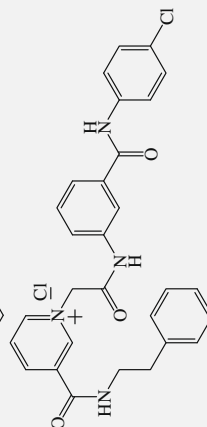
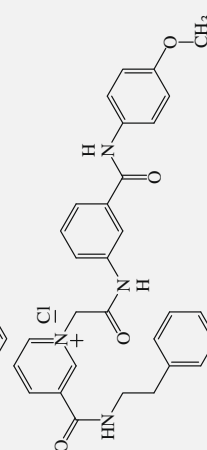
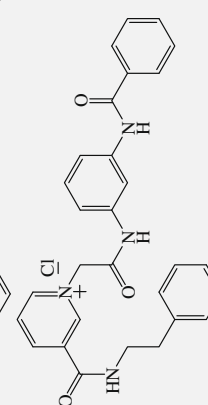
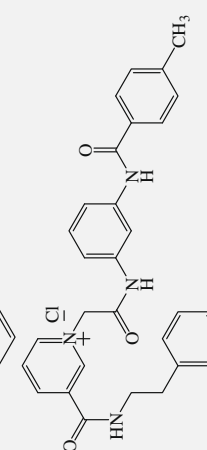
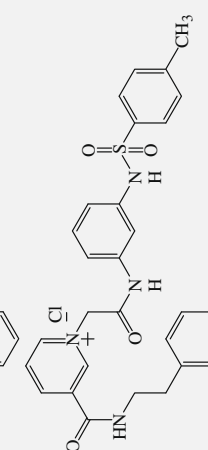
Table 4
The synthesized compounds with their fit values against (Hypo10/10; Hypo 6/18; Hypo 1/21), their corresponding QSAR estimates from Eq. 1 and their in vitro anti-BACE bioactivities

No. ^a	Structure	Fit values ^b			QSAR predictions			Experiments	
		Hypo 10/10	Hypo 6/18	Hypo 1/21	% Inhibition at 50 μ M	IC ₅₀ (μ M)	% Inhibition at 50 μ M ^c	IC ₅₀ (μ M) ^c	
164		0.0	2.1	6.9	88	9.2	42	—	
165		0.0	0.0	6.8	75	13.6	61	—	
166		0.0	0.8	7.2	73	14.7	100	1.0 (98%) ^d	
167		0.0	1.3	7.1	76	12.9	100	3.7 (99%) ^d	
168		0.0	0.0	7.0	75	13.5	51	—	
169		0.0	0.0	7.3	76	13.3	68	13.0 (99%) ^d	
170		0.0	1.6	9.2	56	33.4	50	—	
171		7.8	3.7	9.4	100	1.8	69	—	
172		9.1	6.8	9.4	100	0.9	44	—	

173		8.4	2.6	9.0	100	2.8	64	30.2 (88%) ^d
174		6.9	5.0	8.9	100	2.3	100	1.9 (96%) ^d
175		7.3	0.0	8.5	100	6.6	54	44.7 (87%) ^d
176		9.0	4.2	8.3	100	1.5	24	—
177		8.9	5.9	9.6	100	2.8	34	—
178		8.9	3.9	9.6	100	3.8	4	—
179		5.7	1.0	8.9	100	2.3	72	4.0 (97%) ^d

(continued on next page)

Table 4 (continued)

No. ^a	Structure	Fit values ^b			QSAR predictions		Experiments	
		Hypo 10/10	Hypo 6/18	Hypo 1/21	% Inhibition at 50 μ M	IC ₅₀ (μ M)	% Inhibition at 50 μ M ^c	IC ₅₀ (μ M) ^c
180		6.1	0.0	9.4	100	6.1	58	–
181		4.0	1.3	9.4	100	3.0	78	12.0 (88%) ^d
182		4.3	0.8	9.1	89	8.9	44	–
183		5.6	0.0	9.1	89	8.9	55	–
184		6.7	0.9	9.7	100	4.4	100	2.2 (99%) ^d
185		7.1	3.1	8.8	100	6.4	36	–

^a Compound numbers as in Scheme 7.

^b Best-fit values calculated by Eq. 5.

^c Bioactivity values are the average of at least duplicate measurements.

^d Values between brackets represent the correlation coefficients of the corresponding dose–response lines at three concentrations.

resulting 3D structures were utilized as starting conformers for conformational analysis.

4.1.3. Conformational analysis

The molecular flexibilities of the collected compounds were taken into account by considering each compound as a collection of conformers representing different areas of the conformational space accessible to the molecule within a given energy range. Accordingly, the conformational space of each inhibitor (**1–129**, Table A in Supplementary data) was explored adopting the 'best conformer generation' option within CATALYST. Default parameters were employed in the conformation generation procedure, that is, a conformational ensemble was generated with an energy threshold of 20 kcal/mol from the local minimized structure which has the lowest energy level and a maximum limit of 250 conformers per molecule.³⁵

4.1.4. Pharmacophoric hypotheses generation

All 129 molecules with their associated conformational models were regrouped into a spreadsheet. The biological data of the inhibitors were reported with an 'Uncertainty' value of 3, which means that the actual bioactivity of a particular inhibitor is assumed to be situated somewhere in an interval ranging from one-third to three-times the reported bioactivity value of that inhibitor. Typically, CATALYST requires informative training sets that include at least 16 compounds of evenly spread bioactivities over at least three and a half logarithmic cycles. Lesser training lists could lead to chance correlation and thus faulty models.^{39,41,51} Six structurally diverse training subsets (Table 1) were carefully selected from the collected compounds for pharmacophore modeling.

Each training subset was utilized to conduct four modeling runs to explore the pharmacophoric space of BACE inhibitors. Different hypotheses were generated by altering the interfeature spacing and the number of allowed features in the resulting pharmacophores (Table B in Supplementary data).

Pharmacophore modeling employing CATALYST proceeds through three successive phases: the constructive phase, subtractive phase and optimization phase. During the constructive phase, CATALYST generates common conformational alignments among the most-active training compounds. Only molecular alignments based on a maximum of five chemical features are considered. The program identifies a particular compound as being within the most active category if it satisfies Eq. 2:^{39,41,51}

$$(\text{MAct} \times \text{UncMAct}) - (\text{Act}/\text{UncAct}) > 0.0 \quad (2)$$

where 'MAct' is the activity of the most active compound in the training set, 'Unc' is the uncertainty of the compounds and 'Act' is the activity of the training compounds (Table 1).

In the subsequent subtractive phase, CATALYST eliminates some hypotheses that fit inactive training compounds. A particular training compound is defined as being inactive if it satisfies Eq. 3:^{39,41,51}

$$\text{Log}(\text{Act}) - \text{log}(\text{MAct}) > \text{BS} \quad (3)$$

where, 'BS' is the bioactivity spread (equals 3.5 by default, Table 1).

However, in the optimization phase, CATALYST applies fine perturbations in the form of vectored feature rotation, adding new feature and/or removing a feature, to selected hypotheses that survived the subtractive phase, in an attempt to find new models of enhanced bioactivity/mapping correlations. CATALYST selects the highest-ranking models (10 by default) and presents them as the optimal pharmacophore hypotheses resulting from the particular automatic modeling run.

Eventually, our pharmacophore exploration efforts (24 automatic runs, Table 1 and Table B in Supplementary data) culminated in 226 pharmacophore models of variable qualities.

4.1.5. Assessment of the generated hypotheses

When generating hypotheses, CATALYST attempts to minimize a cost function consisting of three terms: Weight cost, error cost and configuration cost.^{35,39–43} Weight cost is a value that increases as the feature weight in a model deviates from an ideal value of 2. The deviation between the estimated activities of the training set and their experimentally determined values adds to the error cost. The activity of any compound can be estimated from a particular hypothesis through Eq. 4:³⁵

$$\text{Log}(\text{Estimated Activity}) = I + \text{Fit} \quad (4)$$

where I = the intercept of the regression line obtained by plotting the log of the biological activity of the training set compounds against the Fit values of the training compounds. The Fit value for any compound is obtained automatically employing Eq. 5:³⁵

$$\text{Fit} = \sum \text{ mapped hypothesis features} \times W[1 - \sum (\text{disp}/\text{tol})^2] \quad (5)$$

where \sum mapped hypothesis features represents the number of pharmacophore features that successfully superimpose (i.e., map or overlap with) corresponding chemical moieties within the fitted compound, W is the weight of the corresponding hypothesis feature spheres. This value is fixed to 1.0 in CATALYST-generated models. disp is the distance between the center of a particular pharmacophoric sphere (feature centroid) and the center of the corresponding superimposed chemical moiety of the fitted compound; tol is the radius of the pharmacophoric feature sphere (known as Tolerance, equals to 1.6 Å by default). $\sum (\text{disp}/\text{tol})^2$ is the summation of $(\text{disp}/\text{tol})^2$ values for all pharmacophoric features that successfully superimpose corresponding chemical functionalities in the fitted compound.³⁵

The third term, that is, the configuration cost, penalizes the complexity of the hypothesis. This is a fixed cost, which is equal to the entropy of the hypothesis space. The more the numbers of features (a maximum of five) in a generated hypothesis, the higher is the entropy with subsequent increase in this cost. The overall cost (total cost) of a hypothesis is calculated by summing over the three cost factors. However, error cost is the main contributor to total cost.

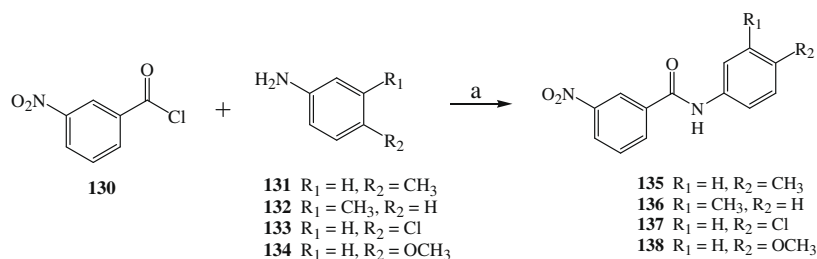
CATALYST also calculates the cost of the null hypothesis, which presumes that there is no relationship in the data and that experimental activities are normally distributed about their mean. Accordingly, the greater the difference from the null hypothesis cost, the more likely that the hypothesis does not reflect a chance correlation. In a successful automatic modeling run, CATALYST ranks the generated models according to their total costs.³⁵

An additional approach to assess the quality of CATALYST-HYPOGEN pharmacophores is to cross-validate them using the CAT-SCRAMBLE program implemented in CATALYST. This validation procedure is based on Fisher's randomization test.⁵¹ In this validation test, a 95% confidence level was selected, which instruct CATALYST to generate 19 random spreadsheets by the CAT-SCRAMBLE command. Subsequently, CATALYST-HYPOGEN is challenged to use these random spreadsheets to generate hypotheses using exactly the same features and parameters used in generating the initial unscrambled hypotheses. Success in generating pharmacophores of comparable cost criteria to those produced by the original unscrambled data reduces the confidence in the training compounds and the unscrambled original pharmacophore models.

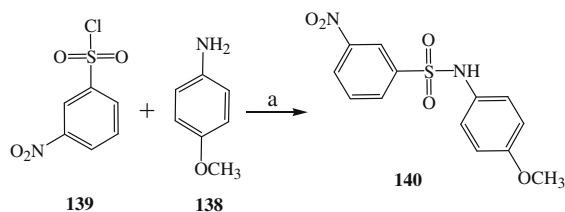
Table C in Supplementary data shows the success criteria of representative pharmacophores from each run.

4.1.6. Clustering of the generated pharmacophore hypotheses

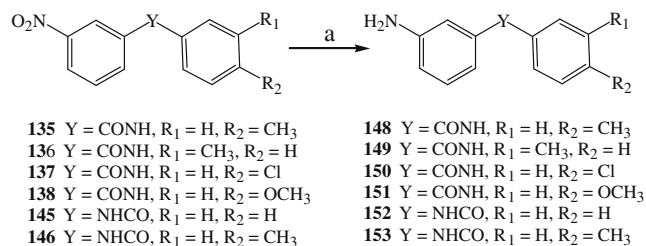
The successful models (226) were clustered into 45 groups utilizing the hierarchical average linkage method available in CATALYST. Therefore, closely-related pharmacophores were grouped in five-



Scheme 1. Synthesis of *N*-phenyl-*m*-nitrobenzamide derivatives: (a) triethylamine in dry acetone.



Scheme 2. Synthesis of *N*-(4-methoxyphenyl)-3-nitro-benzenesulfonamide (**140**): (a) triethylamine and DMAP in dry acetone.



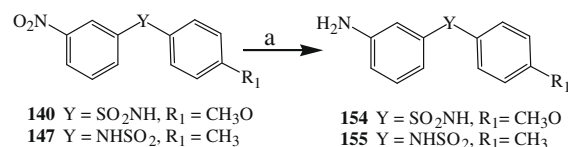
Scheme 4. Reduction of the nitro-phenylbenzamides to their corresponding amine derivatives. (a) $Na_2S_2O_4/Na_2CO_3$ in water.

membered clusters. Subsequently, the highest-ranking representatives, as judged based on their fit-to-bioactivity correlation *F*-values (calculated against collected compounds **1–129**, Table A in Supplementary data and Fig. 1), were selected to represent their corresponding clusters in subsequent QSAR modeling (Table C in Supplementary data).

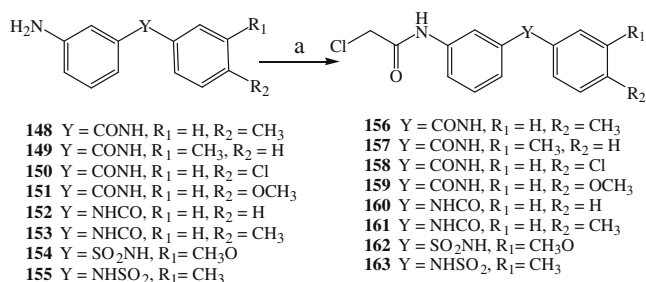
4.1.7. QSAR modeling

A subset of 104 compounds from the total list of inhibitors (**1–129**) was utilized as a training set for QSAR modeling. However, since it is essential to access the predictive power of the resulting QSAR models on an external set of inhibitors, the remaining 25 molecules (ca. 20% of the dataset) were employed as an external test subset for validating the QSAR models. The test molecules were selected as follows: the collected inhibitors (**1–129**, Table A in Supplementary data and Fig. 1) were ranked according to their IC_{50} values, and then every fifth compound was selected for the test set starting from the high-potency end. This selection considers the fact that the test molecules must represent a range of biological activities similar to that of the training set.

The chemical structures of the inhibitors were imported into CERIU2 as standard 3D single conformer representations in SD format. Subsequently, different descriptor groups were calculated for each compound employing the C2.DESRIPTOR module of CERIU2. The calculated descriptors included various simple and valence connectivity indices, electro-topological state indices and other molecular descriptors (e.g., logarithm of partition coefficient, polarizability, dipole moment, molecular volume, molecular

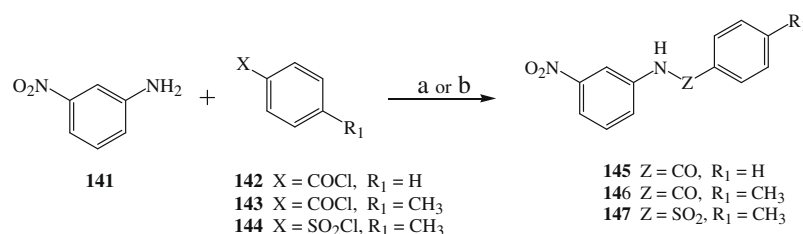


Scheme 5. Reduction of the nitro-phenylbenzulfonamides to their corresponding amine derivatives. (a) $SnCl_2 \cdot 2H_2O$ in ethanol.

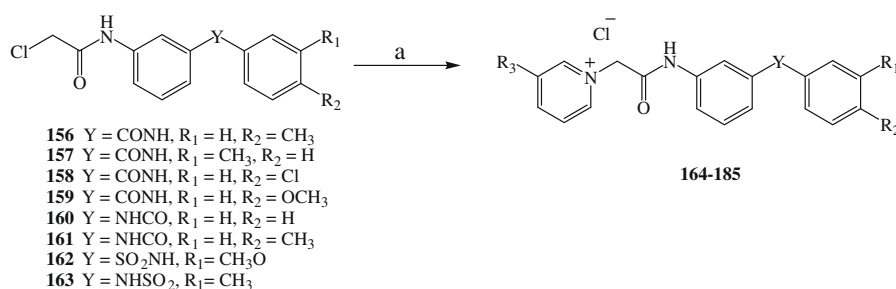


Scheme 6. Synthesis of the *mono*-chloromethyl-acetamido-derivatives (a) *mono*-chloroacetylchloride/triethylamine in dry acetone.

weight, molecular surface area, energies of the lowest and highest occupied molecular orbitals, etc.).⁵¹ Furthermore, the training compounds were fitted (using the Best-fit option in CATALYST) against the representative pharmacophores (45 models, Table C



Scheme 3. Synthesis *N*-(*m*-nitrophenyl)-benzamide and -benzulfonamide derivatives: (a) triethylamine in dry acetone, (b) triethylamine/DMAP in dry acetone.



Scheme 7. Synthesis of the pyridinium acetamido-phenylbenzamides and -phenylbenz sulfonamides (see Table 4 for detailed structures). (a) Fusion with pyridine, nicotinamide or N-phenylethyl nicotinamide (**186**).

Table 5
Inhibitory activities of potent synthesized BACE inhibitors against renin enzyme

Compound	Percent renin inhibition at 50 μM
166	0
167	0
169	0
174	0
179	26
181	26
184	22

in Supplementary data), and their fit values were added as additional descriptors. The fit value for any compound is obtained automatically via Eq. 5.³⁵

Genetic function approximation (GFA) was employed to search for the best possible QSAR regression equation capable of correlating the variations in biological activities of the training compounds with variations in the generated descriptors, that is, multiple linear regression modeling (MLR). The fitness function employed herein is based on Friedman's 'lack-of-fit' (LOF).⁵¹ However, to avoid overwhelming GFA-MLR with large number of poor descriptors; we removed 20% of those showing lowest variance prior to QSAR analysis.

We were obliged to normalize the potencies of the training compounds via division by their corresponding molecular weights, i.e., ligand efficiency ($\frac{\log(1/IC_{50})}{MWT}$),⁵⁴ to achieve reasonable self-consistent QSAR models.

Our preliminary diagnostic trials suggested the following optimal GFA parameters: explore linear, quadratic and spline equations at mating and mutation probabilities of 50%; population size = 500; number of genetic iterations = 30,000 and lack-of-fit (LOF) smoothness parameter = 1.0. However, to determine the optimal number of explanatory terms (QSAR descriptors), it was decided to scan and evaluate all possible QSAR models resulting from 4 to 20 explanatory terms.

All QSAR models were validated employing leave one-out cross-validation (r_{LOO}^2), bootstrapping (r_{BS}^2) and predictive r^2 (r_{PRESS}^2) calculated from the test subsets. The predictive r_{PRESS}^2 is defined as:

$$r_{PRESS}^2 = SD - PRESS/SD \quad (6)$$

where SD is the sum of the squared deviations between the biological activities of the test set and the mean activity of the training set molecules, PRESS is the squared deviations between predicted and actual activity values for every molecule in the test set.

4.1.8. Receiver operating characteristic (ROC) curve analysis

Successful pharmacophore models (i.e., Hypo10/10, Hypo6/18, and Hypo1/21) were further validated by assessing their abilities to selectively capture diverse BACE inhibitors from a large list of decoys employing ROC analysis.

Therefore, it was necessary to prepare valid evaluation structural database (testing set) that contains an appropriate list of decoy compounds in combination with diverse list of known active compounds. The decoy list was prepared as described by Verdonk and co-workers.^{55,56} Briefly, the decoy compounds were selected based on three basic one-dimensional (1D) properties that allow the assessment of distance (D) between two molecules (e.g., i and j), namely: (1) the number of hydrogen-bond donors (NumHBD); (2) number of hydrogen-bond acceptors (NumHBA) and (3) count of nonpolar atoms (NP, defined as the summation of Cl, F, Br, I, S and C atoms in a particular molecule). For each active compound in the testing set, the distance to the nearest other active compound is assessed using their Euclidean Distance (Eq. 7):

$$D(i,j) = \sqrt{(\text{NumHBD}_i - \text{NumHBD}_j)^2 + (\text{NumHBA}_i - \text{NumHBA}_j)^2 + (\text{NP}_i - \text{NP}_j)^2} \quad (7)$$

The minimum distances are then averaged over all active compounds (D_{\min}). Subsequently, for each active compound in the testing set an average of 25 decoys were randomly chosen from the ZINC database.⁵⁷ The decoys were selected in such a way that they did not exceed D_{\min} distance from their corresponding active compound.

Moreover, to further diversify the actives members, that is, to avoid close similarity among actives in the testing set, any active compound having zero distance ($D(i,j)$) from other active compound (s) in the testing set were excluded. Active testing compounds were defined as those possessing BACE-1 affinities (IC_{50} values) ranging from 2 nM to 10 μM. The testing set included 25 active compounds and 617 ZINC compounds.

The testing set (642 compounds) was screened by each particular pharmacophore for ROC analysis employing the 'Best flexible search' option implemented in CATALYST, while the conformational spaces of the compounds were generated employing the 'Fast conformation generation option' implemented in CATALYST. Compounds missing one or more features were discarded from hit lists. The in silico hits were scored employing their fit values (best fit values) as calculated by Eq. 5.

ROC curve analysis describes the sensitivity (Se or true positive rate, Eq. 8) for any possible change in the number of selected compounds (n) as a function of $(1 - Sp)$. Sp is defined as specificity or true negative rate (Eq. 9):^{55,58}

$$Se = \frac{\text{Number of Selected Actives}}{\text{Total Number of Actives}} = \frac{TP}{TP + FN} \quad (8)$$

$$Sp = \frac{\text{Number of Discarded Inactives}}{\text{Total Number of Inactives}} = \frac{TN}{TN + FP} \quad (9)$$

where, TP is the number of active compounds captured by the virtual screening method (true positives), FN is the number of active compounds discarded by the virtual screening method, TN is the

number of discarded decoys (presumably inactives), while FP is the number of captured decoys (presumably inactives).

A ROC curve is plotted by setting the score of the active molecule as the first threshold. Afterwards, the number of decoys within this cutoff is counted and the corresponding Se and Sp pair is calculated. This calculation is repeated for the active molecule with the second highest score and so forth, until the scores of all actives are considered as selection thresholds.^{55,58}

The ROC curve representing ideal distributions, where no overlap between the scores of active molecules and decoys exists, proceeds from the origin to the upper-left corner until all the actives are retrieved and Se reaches the value of 1. Thus, the ideal ROC curve continues as a horizontal straight line to the upper-right corner where all actives and all decoys are retrieved, which corresponds to Se = 1 and Sp = 0. In contrast to that, the ROC curve for a set of actives and decoys with randomly distributed scores tends towards the Se = 1 – Sp line asymptotically with increasing number of actives and decoys.⁵⁵

The success of a particular virtual screening workflow can be judged from the following criteria:

- (1) Area under the ROC curve (AUC).⁵⁸ In an optimal ROC curve an AUC value of 1 is obtained; however, random distributions cause an AUC value of 0.5. Virtual screening that performs better than a random discrimination of actives and decoys retrieve an AUC value between 0.5 and 1.^{55,58}
- (2) Overall accuracy (ACC): describes the percentage of correctly classified molecules by the screening protocol (10). Testing compounds are assigned a binary score value of zero (compound not captured) or one (compound captured):^{55,59,60}

$$ACC = \frac{TP + TN}{N} = \frac{A}{N} \cdot Se + \left(1 - \frac{A}{N}\right) \cdot Sp \quad (10)$$

where *N* is the total number of compounds in the testing database, *A* is the number of true actives in the testing database.

- (3) Overall specificity (SPC): describes the percentage of discarded inactives by the particular virtual screening workflow. Inactive test compounds are assigned a binary score value of zero (compound not captured) or one (compound captured).^{55,59,60}
- (4) Overall true positive rate (TPR or overall sensitivity): describes the fraction percentage of captured actives from the total number of actives. Active test compounds are assigned a binary score value of zero (compound not captured) or one (compound captured).
- (5) Overall false negative rate (FNR or overall percentage of discarded actives): describes the fraction percentage of active compounds discarded by the virtual screening method. Discarded active test compounds are assigned a binary score value of zero (compound not captured) or one (compound captured).

4.2. Synthetic procedures

Melting points were measured using Gallenkamp melting point apparatus and are uncorrected. ¹H NMR and ¹³C NMR spectrums were collected on a Varian Oxford NMR300 spectrometer. High resolution mass spectrometry was performed using LC Mass Bruker Apex-IV mass spectrometer utilizing an electrospray interface. Infrared spectra were recorded using Shimadzu IR Affinity-1 spectrophotometer. The samples were dissolved in CHCl₃ and analyzed as thin solid films using NaCl plates or as KBr pellets. Analytical thin layer chromatography (TLC) was carried out using pre-coated aluminum plates and visualized by UV light (at 254 and/or

360 nm). Elemental analysis was performed using EuroVector elemental analyzer. Chemicals and solvents were used without further purification.

4.2.1. Preparation of *N*-(3-nitrophenyl)benzamide derivatives (135–138)

To a magnetically-stirred, ice-bathed, solution of the substituted aniline and triethylamine (2 equiv) in dry acetone (50 mL), benzoyl chloride (2 equiv) in acetone was added. The solution was stirred at room temperature until completion (as revealed by TLC). The reaction mixture was quenched by slow addition into sufficient 5% aqueous sodium bicarbonate solution to neutralize all generated acid. The precipitated crude *N*-(3-nitrophenyl)benzamide products were purified by recrystallization from acetone/water (Scheme 1).⁶¹

4.2.1.1. 3-Nitro-*N*-*p*-tolyl-benzamide (135). Prepared from commercially available 3-nitrobenzoyl chloride **130** (25.9 g, 0.14 mol) dissolved in acetone (50 mL) and *p*-tolylamine **131** (10.0 g, 0.09 mol) to yield **135** as white crystalline powder (20.0 g, 87%) mp: 160–161 °C; ν_{\max} (KBr disc) 3298, 1647, 1527 cm⁻¹; ¹H NMR (300 MHz, DMSO-*d*₆): δ 2.26 (s, 3H), 7.15 (d, 2H, *J* 7.8 Hz), 7.63 (d, 2H, *J* 7.5 Hz), 7.79 (t, 1H), 8.39 (t, 2H), 8.75 (s, 1H), 10.49 (s, 1H, NH) ppm; ¹³C NMR (75 MHz, DMSO-*d*₆): δ 21.20 (CH₃), 121.25 (2 × CH), 123.05 (CH), 126.76 (CH), 129.78 (2 × CH), 130.84 (CH), 133.84 (C), 134.81 (CH), 136.82 (C), 137.01 (C), 148.41 (C), 163.76 (C=O) ppm; HRMS-ESI *m/z* [M+Na]⁺ calcd for C₁₄H₁₂N₂NaO₃: 279.07456, found: 279.07401.

4.2.1.2. 3-Nitro-*N*-*m*-tolyl-benzamide (136). Prepared from **130** (25.9 g, 0.14 mol) and *m*-tolylamine **132** (10 g, 0.09 mol) to yield **136** as white crystalline powder (20.0 g, 87%), mp 115 °C; ν_{\max} (KBr disc) 3294, 1647, 1531 cm⁻¹; ¹H NMR (300 MHz, DMSO-*d*₆): δ 2.29 (s, 3H, CH₃), 6.93 (d, 1H, *J* 7.5 Hz), 7.23 (t, 1H), 7.55 (d, 1H, *J* 7.8 Hz), 7.58 (s, 1H), 7.80 (t, 1H), 8.37 (d, 1H, *J* 9.9 Hz), 8.41 (d, 1H, *J* 6 Hz), 8.75 (s, 1H), 10.49 (s, 1H, NH); ¹³C NMR (75 MHz, DMSO-*d*₆): δ 21.86 (CH₃), 118.42 (CH), 121.77 (CH), 123.06 (CH), 125.54 (CH), 126.23 (CH), 129.23 (CH), 130.87 (CH), 134.82 (CH), 136.69 (C), 138.54 (C), 139.24 (C), 148.40 (C), 163.94 (C=O) ppm; HRMS-ESI *m/z* [M-H]⁺ calcd for C₁₄H₁₁N₂O₃: 255.07697, found: 255.07752.

4.2.1.3. *N*-(4-Chloro-phenyl)-3-nitro-benzamide (137). Prepared from **130** (28.94 g, 0.16 mol) and 4-chloro-phenylamine **133** (10.0 g, 0.08 mol) to yield **137** as white crystalline powder (20.0 g, 91%) mp: 173–175 °C; ν_{\max} (KBr disc) 3290, 1651, 1527 cm⁻¹; ¹H NMR (300 MHz, DMSO-*d*₆): δ 7.37 (d, 2H, *J* 9.3 Hz), 7.79 (d, 2H, *J* 8.7 Hz), 7.79 (t, 1H), 8.37 (d, 1H, *J* 6.9 Hz), 8.41 (d, 1H, *J* 8.1 Hz), 8.75 (s, 1H), 10.68 (s, 1H) ppm; ¹³C NMR (75 MHz, DMSO-*d*₆): δ 122.76 (2 × CH), 123.11 (CH), 126.99 (CH), 128.47 (C), 129.31 (2 × CH), 130.93 (CH), 134.88 (CH), 136.66 (C), 138.33 (C), 148.41 (C), 164.12 (C=O) ppm; HRMS-ESI *m/z* [M+H]⁺ calcd for C₁₃H₁₀ClN₂O₃: 277.03799, found: 277.03745.

4.2.1.4. *N*-(4-Methoxy-phenyl)-3-nitro-benzamide (138). Prepared from **130** (14.0 g, 0.08 mol) and 4-methoxy-phenylamine **134** (4.6 g, 0.038 mol) to yield **138** as yellowish-green crystalline powder (4.87 g, 47%) mp: 176–177 °C; ν_{\max} (KBr disc) 3298, 1647, 1527 cm⁻¹; ¹H NMR (300 MHz, DMSO-*d*₆): δ 3.73 (s, 3H), 6.94 (d, 2H, *J* 9 Hz), 7.67 (d, 2H, *J* 9.3), 7.811 (t, 1H), 7.37 (d, 1H, *J* 6.6), 8.40 (d, 1H, *J* 7.2), 8.76 (s, 1H), 10.46 (s, 1H) ppm; ¹³C NMR (75 MHz, DMSO-*d*₆): δ 55.87 (CH₃), 114.50 (2 × CH), 122.85 (2 × CH), 122.99 (CH), 126.71 (CH), 130.85 (CH), 132.37 (C), 134.76 (CH), 137.04 (C), 148.43 (C), 156.53 (C), 163.53 (C=O) ppm; HRMS-ESI *m/z* [M-H]⁺ calcd for C₁₄H₁₁N₂O₄: 271.07188, found: 271.07243.

4.2.2. Preparation of *N*-(4-methoxyphenyl)-3-nitro-benzene-sulfonamide and *N*-(*m*-nitrophenyl)-benzulfonamide derivatives (**140**, **145**–**147**)

To a magnetically-stirred, ice-bathed, solution containing the substituted aniline (1.0 equiv) and triethylamine (2 equiv) in dry acetone (50 mL), a solution of 3-nitro-benzenesulfonyl chloride (1.5–2.0 equiv) and DMAP (0.5 equiv) in dry acetone (50 mL) was added. The reaction was stirred at room temperature overnight until TLC revealed all aniline had reacted. The reaction mixture was quenched by slow addition onto sufficient 5% aqueous sodium bicarbonate to neutralize all generated acid. The precipitated crude products were purified by recrystallization from acetone/water (Schemes 2 and 3).⁶²

4.2.2.1. *N*-(4-Methoxy-phenyl)-3-nitro-benzenesulfonamide (**140**).

Prepared from commercially available 3-nitro-benzenesulfonyl chloride **139** (7.0 g, 0.0315 mol) and 4-methoxy-phenylamine **138** (3.88 g, 0.0315 mol) to yield **140** as white powder (3.59 g, 37%) mp: 193–194 °C; ν_{\max} (KBr disc) 3448, 1604 cm^{-1} ; ^1H NMR (300 MHz, DMSO- d_6): δ 3.70 (s, 3H), 6.97 (d, 1H, J 6 Hz), 7.05 (d, 1H, J 9 Hz), 7.98 (t, 1H), 8.23 (d, 1H, J 9 Hz), 8.64 (s, 1H), 8.64 (d, 1H, J 9 Hz) ppm; ^{13}C NMR (75 MHz, DMSO- d_6): δ 56.30 (CH₃), 115.77 (2 × CH), 123.49 (2 × CH), 125.39 (CH), 130.16 (CH), 132.55 (CH), 133.42 (C), 134.63 (C), 140.03 (C), 148.71 (C), 161.68 (C=O) ppm; HRMS-ESI m/z [$M-H$]⁺ calcd for C₁₃H₁₁N₂O₅S: 308.04222, found: 308.04275.

4.2.2.2. *N*-(3-Nitrophenyl)-benzamide (**145**).

Prepared from commercially available 3-nitroaniline **141** (12.0 g, 0.09 mol) and benzoyl chloride **142** (24.0 g, 0.17 mol) to yield **145** as light yellow crystalline powder (20 g, 92%) mp: 157–160 °C; ν_{\max} (thin film) 1651, 1539 cm^{-1} ; ^1H NMR (300 MHz, CDCl₃): δ 7.2 (s, 1H), 7.47–7.58 (m, 5H), 7.88 (d, 1H, J 7.2 Hz), 7.99 (d, 1H, J 8.4 Hz), 8.116 (m, 1H), 8.49 ppm (s, 1H); ^{13}C -NMR (CDCl₃): δ 113.91 (CH), 118.10 (CH), 124.85 (CH), 126.08 (2 × CH), 127.95 (2 × CH), 128.93 (CH), 131.45 (CH), 132.96 (C), 138.03 (C), 147.57 (C), 164.92 (C=O); HRMS-ESI m/z [$M-H$]⁺ calcd for C₁₃H₉N₂O₃: 241.06132, found 241.06187.

4.2.2.3. 4-Methyl-*N*-(3-nitro-phenyl)-benzamide (**146**).

Prepared from **141** (6.0 g, 0.05 mol) and 4-methyl benzoylchloride **143** (12.0 g, 0.09 mol) to yield **146** as light yellow crystalline powder (13.3 g, 63%) mp: 175 °C; ν_{\max} (thin film) 1654, 1523 cm^{-1} ; ^1H NMR (CDCl₃): δ 8.78 (s, 1H), 8.776 (s, 1H), 8.16 (dd, 1H, J 7.2, 0.9 Hz), 7.9 (d, 1H, J 1.2 Hz), 7.88 (d, 2H, J 7.8 Hz), 7.60 (m, 1H), 7.32 (dd, 2H, J 8.1 Hz), 2.28 (s, 3H) ppm; ^{13}C NMR (CDCl₃): δ 21.71 (CH₃), 114.93 (CH), 118.64 (CH), 126.76 (CH), 128.49 (2 × CH), 129.69 (2 × CH), 130.66 (CH), 131.97 (C), 141.14 (C), 142.85 (C), 148.52 (C), 166.48 (C=O) ppm; HRMS-ESI m/z [$M+H$]⁺ calcd for C₁₄H₁₂N₂NaO₃: 279.07456, found: 279.07401.

4.2.2.4. 4-Methyl-*N*-(3-nitro-phenyl)-benzenesulfonamide (**147**).

Prepared from **141** (10.0 g, 50 mmol) and 4-methyl benzenesulfonyl chloride **144** (15.0 g, 78 mmol) to yield **147** as white crystalline powder (11.1 g, 75%) mp: 182–185 °C; ν_{\max} (KBr disc) 3580, 1535, 1381, 1350 cm^{-1} ; ^1H NMR (CDCl₃): δ 2.4 (s, 3H), 7.36 (m, 3H), 7.554 (t, 1H), 7.791 (d, 1H, J 8.4 Hz), 7.88 (s, 2H), 8.3 (d, 2H, J 7.2 Hz); ^{13}C NMR (CDCl₃): δ 22.00 (CH₃), 125.23 (CH), 126.91 (CH), 128.79 (2 × CH), 130.13 (2 × CH), 130.16 (CH), 135.86 (C), 136.15 (C), 137.94 (CH), 146.00 (C), 148.66 (C) ppm; HRMS-ESI m/z [$M-H$]⁺ calcd for C₁₃H₁₁N₂O₄S: 292.04731, found: 292.04786.

4.2.3. Reduction of nitro-phenylbenzamide derivatives (**148**–**153**)

To a magnetically-stirred aqueous suspension of the particular nitro-phenylbenzamide (1.0 equiv in 300 mL), Na₂S₂O₄ (5.0 equiv)

and Na₂CO₃ (7.0 equiv) were added as dry powders. The reaction mixture was stirred at room temperature for seven days. The reaction mixture was supplemented with Na₂S₂O₄ (2.0 equiv) every 48 h until thin-layer chromatography revealed that all starting material had reacted. The reaction was terminated by filtration. The solid residue was rinsed with water (200 mL) over 2–3 h and dried under vacuum (Scheme 4).⁶³

4.2.3.1. 3-Amino-*N*-*p*-tolyl-benzamide (**148**).

Prepared from compound **135** (23.0 g, 0.089 mol) to yield **148** as white powder (2.82 g, 14%) mp: 165–167 °C; ν_{\max} (KBr disc) 3479, 3387, 3286, 1651 cm^{-1} ; ^1H NMR (300 MHz, DMSO- d_6): δ 2.24 (s, 3H), 5.28 (s, 2H), 6.70 (d, 1H, J 7.8), 7.00–7.13 (m, 5H), 7.54 (d, 2H, J 8.1), 9.96 (s, 1H) ppm; ^{13}C NMR (75 MHz, DMSO- d_6): δ 21.17 (CH₃), 113.61 (CH), 115.32 (CH), 117.32 (CH), 120.86 (2 × CH), 129.4 (CH), 129.60 (2 × CH), 132.93 (C), 136.71 (C), 137.54 (C), 149.43 (C), 166.85 (C=O) ppm; HRMS-ESI m/z [$M+H$]⁺ calcd for C₁₄H₁₅N₂O: 228.12179, found: 228.12125.

4.2.3.2. 3-Amino-*N*-*m*-tolyl-benzamide (**149**).

Prepared from compound **136** (20.0 g, 0.078 mol) as white powder (3.97 g, 22%) mp: 95–96 °C; ν_{\max} (KBr disc) 3421, 3336, 3255, 1647 cm^{-1} ; ^1H NMR (300 MHz, DMSO- d_6): δ 2.27 (s, 3H), 5.29 (s, 2H), 6.71 (d, 1H, J 7.2 Hz), 6.86 (d, 1H, J 7.5 Hz), 7.70–7.20 (m, 4H), 7.51 (d, 1H, J 7.8 Hz), 7.58 (s, 1H), 9.96 (s, 1H) ppm; ^{13}C NMR (75 MHz, DMSO- d_6): δ 21.93 (CH₃), 113.63 (CH), 115.36 (CH), 117.38 (CH), 118.06 (CH), 121.39 (CH), 124.75 (CH), 129.06 (CH), 129.06 (CH), 136.69 (C), 138.32 (C), 139.97 (C), 149.44 (C), 167.00 (C=O) ppm; HRMS-ESI m/z [$M+H$]⁺ calcd for C₁₄H₁₅N₂O: 228.12179, found: 228.12125.

4.2.3.3. 3-Amino-*N*-(4-chloro-phenyl)-benzamide (**150**).

Prepared from compound **137** (25.0 g, 0.09 mol) to yield **150** as white powder (2.92 g, 13%) mp: 175–177 °C; ν_{\max} (KBr disc) 3402, 3321, 1651 cm^{-1} ; ^1H NMR (300 MHz, DMSO- d_6): δ 5.31 (s, 2H), 6.73 (d, 1H, J 7.2 Hz), 7.01–7.14 (m, 3H), 7.35 (d, 2H, J 8.6 Hz), 7.77 (d, 2H, J 8.7 Hz), 10.18 (s, 1H) ppm; ^{13}C NMR (75 MHz, DMSO- d_6): δ 113.60 (CH), 115.38 (CH), 117.58 (CH), 122.32 (2 × CH), 127.62 (C), 129.14 (2 × CH), 129.50 (CH), 136.33 (C), 139.04 (C), 149.49 (C), 167.17 (C=O) ppm; HRMS-ESI m/z [$M+H$]⁺ calcd for C₁₃H₁₂ClN₂O: 247.06381, found: 247.06327.

4.2.3.4. 3-Amino-*N*-(4-methoxy-phenyl)-benzamide (**151**).

Prepared from compound **138** (4.87 g, 0.019 mol) to yield **151** as grey powder (1.58 g, 34%) mp: 202–204 °C; ν_{\max} (KBr disc) 3387, 3321, 1651 cm^{-1} ; ^1H NMR (300 MHz, DMSO- d_6): δ 3.72 (s, 3H), 5.29 (s, 2H), 6.71 (dd, 1H, J 0.9, 7.2 Hz), 6.88 (d, 2H, J 9 Hz), 7.00–7.19 (m, 3H), 7.62 (dd, 2H, J 2.1, 4.8 Hz), 9.92 (s, 1H) ppm; ^{13}C NMR (75 MHz, DMSO- d_6): δ 55.82 (CH₃), 113.60 (CH), 114.34 (2 × CH), 115.29 (CH), 117.28 (CH), 122.44 (2 × CH), 129.40 (CH), 133.14 (C), 136.70 (C), 149.40 (C), 156.00 (C), 166.61 (C=O) ppm; HRMS-ESI m/z [$M+H$]⁺ calcd for C₁₄H₁₅N₂O₂: 244.11671, found: 244.11616.

4.2.3.5. *N*-(3-Amino-phenyl)-benzamide (**152**).

This compound was prepared from **145** (9.2 g, 0.04 mol) to yield **152** as white powder (5.2 g, 49%) mp: 124 °C; ν_{\max} (thin film) 3587, 1651, 1543, 1458 cm^{-1} ; ^1H NMR (CDCl₃): δ 3.61 (s, 2H), 6.43 (dd, 1H, J 7.8, 0.9 Hz), 6.84 (dd, 1H, J 7.8, 0.9 Hz), 7.08 (t, 1H), 7.23–7.49 (m, 5H), 7.80 (d, 2H, J 5.25 Hz); ^{13}C NMR (CDCl₃): δ 107.31 (CH), 110.56 (CH), 111.60 (CH), 127.35 (2 × CH), 128.89 (2 × CH), 129.96 (CH), 131.91 (CH), 135.34 (C), 139.27 (C), 147.56 (C), 166.27 (C=O) ppm; HRMS-ESI m/z [$M+H$]⁺ calcd for C₁₃H₁₃N₂O: 213.10279, found: 213.10224.

4.2.3.6. N-(3-Amino-phenyl)-4-methyl-benzamide (153). Prepared from **146** (6.5 g, 0.025 mol) to yield **153** as white powder (1.9 g, 34%) mp: 138–139 °C; ν_{\max} (thin film) 3564, 1650, 1616 cm^{-1} ; ^1H NMR (CDCl_3): δ 2.35 (s, 3H), 5.06 (s, 2H), 6.27 (d, 1H, J 7.2 Hz), 6.83 (d, 1H, J 7.5 Hz), 6.91 (m, 1H), 7.08 (s, 1H), 7.28 (d, 2H, J 7.8 Hz), 7.81 (d, 2H, J 7.8 Hz), 9.84 (s, 1H); ^{13}C NMR (CDCl_3): δ 21.66 (CH_3), 106.75 (CH), 109.02 (CH), 110.31 (CH), 128.32 ($2 \times \text{CH}$), 129.44 ($2 \times \text{CH}$), 129.50 (CH), 133.07 (C), 140.47 (C), 141.95 (C), 149.58 (C), 165.76 (C=O) ppm; HRMS-ESI m/z [$M+\text{H}$] $^+$ calcd for $\text{C}_{14}\text{H}_{15}\text{N}_2\text{O}$: 228.12179, found: 228.12124.

4.2.4. Reduction nitro-phenylbenzulfonamides derivatives (154, 155)

To a magnetically-stirred suspension of the particular nitro-phenylbenzulfonamide derivative (1.0 equiv) in anhydrous ethanol (100 ml), $\text{SnCl}_2 \cdot 2\text{H}_2\text{O}$ (5.0 equiv) was added. The reaction mixture heated to reflux for 2 h then allowed to cool at room temperature; poured onto ice (100 mL) and made slightly basic (pH 8.5) by addition of saturated NaHCO_3 solution. Subsequently, solid NaCl (ca. 1.0 g) was added and the resulting mixture was extracted with ethyl acetate (3×100 mL). The organic layers were combined and washed thoroughly with brine (3×50 mL) and dried over anhydrous MgSO_4 . Finally, ethyl acetate was evaporated under reduced pressure to yield the free base of the title compounds (Scheme 5).^{64,65}

4.2.4.1. 3-Amino-N-(4-methoxy-phenyl)-benzenesulfonamide (154). Prepared from compound **140** (3.11 g, 0.01 mol) to yield **154** as brown powder (1.49 g, 53%) mp: 154–155 °C; ν_{\max} (KBr disc) 3448, 3371, 1635, 1600 cm^{-1} ; ^{13}C NMR (75 MHz, $\text{DMSO}-d_6$): δ 56.15 (CH_3), 112.60 (CH), 114.86 ($2 \times \text{CH}$), 115.06 ($2 \times \text{CH}$), 119.53 (CH), 126.71 (C), 130.38 (CH), 133.29 (CH), 140.09 (C), 150.18 (C), 160.94 (C=O) ppm; HRMS-ESI m/z [M] $^+$ calcd for $\text{C}_{13}\text{H}_{14}\text{N}_2\text{O}_3\text{S}$: 279.07587, found: 279.07532.

4.2.4.2. N-(3-Amino-phenyl)-4-methyl-benzenesulfonamide (155). Prepared from **147** (8.8 g, 0.03 mol) to yield **155** as brown powder (4.0 g, 51%) mp: 230–233 °C; ν_{\max} (thin film) 3564, 1519 cm^{-1} ; ^1H NMR (300 MHz, $\text{DMSO}-d_6$): δ 2.479 (s, 3H), 5.35 (s, 2H, D_2O exchangeable, NH_2), 5.99 (dd, 1H, J 7.8, 0.9 Hz), 6.30 (s, 1H), 6.61 (dd, 1H, J 8.2, 1.5 Hz), 6.97 (t, 1H), 7.45 (d, 2H, J 8.1 Hz), 7.67 (d, 2H, J 8.25 Hz), 7.70 (s, D exchangeable, 1H) ppm; ^{13}C NMR (75 MHz, $\text{DMSO}-d_6$): δ 21.86 (CH_3), 116.14 (CH), 116.95 (CH), 118.57 (CH), 128.68 ($2 \times \text{CH}$), 129.98 ($2 \times \text{CH}$), 130.49 (CH), 134.95 (C), 136.85 (C), 145.80 (C), 150.50 (C) ppm; HRMS-ESI m/z [$M-\text{H}$] $^+$ calcd for $\text{C}_{13}\text{H}_{13}\text{N}_2\text{O}_2\text{S}$: 261.06977, found: 261.13107.

4.2.5. Synthesis of the mono-chloromethyl-acetamido derivatives (156–163)

To a magnetically-stirred, ice-bathed, solution or suspension of the particular aniline (**148–155**, 1.0 equiv) and triethylamine (2.0 equiv) in dry acetone (75 mL), 2-chloroacetyl chloride (1.0 equiv) in dry acetone (100 mL) was gradually added over 30 min. The reaction mixture was stirred at room temperature until TLC revealed complete consumption of the starting aniline. Subsequently, the reaction mixture was poured slowly onto sufficient 5% aqueous sodium bicarbonate to neutralize the generated acid. The precipitated crude products were purified by recrystallization from acetone/water (Scheme 6).⁶⁶

4.2.5.1. 3-(2-Chloro-acetylamino)-N-p-tolyl-benzamide (156). Prepared from compound **148** (2.82 g, 0.0125 mol) to yield **156** as grey crystalline powder (2.02 g, 53%) mp: 228 (decomp.) °C; ν_{\max} (KBr disc) 3448, 1670, 1647, 1597 cm^{-1} ; ^1H NMR (300 MHz, $\text{DMSO}-d_6$): δ 2.25 (s, 3H), 4.26 (s, 2H), 7.12 (d, 2H, J 7.8 Hz), 7.46

(t, 1H), 7.62 (d, 2H, J 7.8 Hz), 7.65 (d, 1H, J 6.6 Hz), 7.81 (d, 1H, J 7.8 Hz), 8.06 (s, 1H), 10.19 (s, 1H), 10.5 (s, 1H) ppm; ^{13}C NMR (75 MHz, $\text{DMSO}-d_6$): δ 21.19 (CH_3), 44.23 (CH_2), 119.52 (CH), 121.02 ($2 \times \text{CH}$), 122.85 (CH), 123.41 (CH), 129.64 ($2 \times \text{CH}$), 133.33 (C), 136.60 (C), 137.26 (C), 139.29 (C), 165.57 (C=O), 165.84 (C=O) ppm; HRMS-ESI m/z [$M+\text{Na}$] $^+$ calcd for $\text{C}_{16}\text{H}_{15}\text{ClN}_2\text{NaO}_2$: 325.07197, found: 325.07143.

4.2.5.2. 3-(2-Chloro-acetylamino)-N-m-tolyl-benzamide (157). Prepared from compound **149** (3.7 g, 0.016 mol) to yield **157** as grey crystalline powder (1.65 g, 34%) mp: 208–209 °C; ν_{\max} (KBr disc) 3259, 1670, 1651, 1597 cm^{-1} ; ^1H NMR (300 MHz, $\text{DMSO}-d_6$): δ 2.28 (s, 3H), 4.26 (s, 2H), 6.90 (d, 1H, J 7.2 Hz), 7.2 (t, 1H), 7.45 (d, 1H, J 8.1 Hz), 7.49 (t, 1H), 7.58 (s, 1H), 7.64 (d, 1H, J 6.6 Hz), 7.8 (d, 1H, J 7.8 Hz), 8.06 (s, 1H), 10.19 (s, 1H), 10.5 (s, 1H) ppm; ^{13}C NMR (75 MHz, $\text{DMSO}-d_6$): δ 21.92 (CH_3), 44.23 (CH_2), 118.21 (CH), 119.53 (CH), 121.54 (CH), 122.91 (CH), 123.43 (CH), 125.09 (CH), 129.14 (CH), 129.61 (CH), 136.57 (C), 138.44 (C), 139.30 (C), 139.7 (C), 165.57 (C=O), 165.98 (C=O) ppm; HRMS-ESI m/z [$M+\text{Na}$] $^+$ calcd for $\text{C}_{16}\text{H}_{15}\text{ClN}_2\text{NaO}_2$: 325.07197, found: 325.07143.

4.2.5.3. 3-(2-Chloro-acetylamino)-N-(4-chloro-phenyl)-benzamide (158). Prepared from compound **150** (2.5 g, 0.018 mol) to yield **158** as light brown powder (4.5 g, 77%) mp: 245–246 °C; ν_{\max} (KBr disc) 3282, 1670, 1651, 1593 cm^{-1} ; ^1H NMR (300 MHz, $\text{DMSO}-d_6$): δ 4.24 (s, 2H), 7.40 (d, 2H, J 4.98 Hz), 7.48 (t, 1H), 7.64 (d, 1H, J 5.2 Hz), 7.78 (d, 2H, J 4.98 Hz), 7.82 (d, 1H, J 6.4 Hz), 8.09 (s, 1H), 10.4 (s, 1H), 10.54 (s, 1H) ppm; ^{13}C NMR (75 MHz, $\text{DMSO}-d_6$): δ 44.23 (CH_2), 119.53 (CH), 122.50 ($2 \times \text{CH}$), 123.09 (CH), 123.49 (CH), 127.98 (C), 129.23 ($2 \times \text{CH}$), 129.68 (CH), 136.23 (C), 138.77 (C), 139.36 (C), 165.61 (C=O), 166.16 (C=O) ppm; [$M+\text{Na}$] $^+$ found 345.01680 $\text{C}_{15}\text{H}_{12}\text{Cl}_2\text{N}_2\text{NaO}_2$ requires 345.01735.

4.2.5.4. 3-(2-Chloro-acetylamino)-N-(4-methoxy-phenyl)-benzamide (159). Prepared from compound **151** (1.49 g, 6.2 mmol) to yield **159** as white powder (0.74 g, 37%) mp: 242–242 °C; ν_{\max} (KBr disc) 3305, 1674, 1647, 1593 cm^{-1} ; ^1H NMR (300 MHz, $\text{DMSO}-d_6$): δ 3.72 (s, 3H), 4.26 (s, 2H), 6.90 (dd, 2H, J 1.5, 5.1 Hz), 7.45 (t, 1H), 7.63 (d, 3H, J 8.4 Hz), 7.78 (d, 1H, J 7.2 Hz), 8.06 (s, 1H), 10.15 (s, 1H), 10.50 (s, 1H) ppm; HRMS-ESI m/z [$M+\text{Na}$] $^+$ calcd for $\text{C}_{16}\text{H}_{15}\text{ClN}_2\text{NaO}_3$: 341.06689, found: 341.06634.

4.2.5.5. N-[3-(2-Chloro-acetylamino)-phenyl]-benzamide (160). Prepared from **152** (5.8 g, 0.027 mol) to yield **160** as white powder (5.1 g, 69%) mp: 240–243 °C; ν_{\max} (thin film) 3286, 1670, 1647 cm^{-1} ; ^1H NMR (300 MHz, $\text{DMSO}-d_6$): δ 4.26 (s, 2H), 7.27–8.16 (m, 9H), 10.33 (s, 1H), 10.38 (s, 1H); ^{13}C -NMR (DMSO): δ 44.34 (CH_2), 112.19 (CH), 115.49 (CH), 116.69 (CH), 128.41 ($2 \times \text{CH}$), 129.06 ($2 \times \text{CH}$), 129, 63 (CH), 132.29 (CH), 135.60 (C), 139.38 (C), 140.28 (C), 165.33 (C=O), 166.34 (C=O) ppm; HRMS-ESI m/z [$M+\text{Na}$] $^+$ calcd for $\text{C}_{15}\text{H}_{13}\text{ClN}_2\text{NaO}_2$: 311.05632, found: 311.05913.

4.2.5.6. N-[3-(2-Chloro-acetylamino)-phenyl]-4-methyl-benzamide (161). Prepared from **153** (1.5 g, 6.6 mmol) to yield **161** as pale yellow powder (1.3 g, 67%) mp: 233–235 °C; ν_{\max} (thin film) 3502, 1651, 1539 cm^{-1} ; ^1H NMR (300 MHz, $\text{DMSO}-d_6$): δ 2.36 (s, 3H), 4.23 (s, 2H), 7.26–7.32 (m, 5H), 7.42 (s, 1H), 7.85 (d, 1H, J 7.8 Hz), 8.11 (s, 1H), 10.21 (s, 1H), 10.34 (s, 1H) ppm; ^{13}C NMR (75 MHz, $\text{DMSO}-d_6$): δ 21.70 (CH_3), 44.31 (CH_2), 112.16 (CH), 115.34 (CH), 116.65 (CH), 128.42 ($2 \times \text{CH}$), 129.57 ($2 \times \text{CH}$), 132.65 (C), 139, 31 (C), 140.31 (C), 142.30 (C), 165.28 (C=O), 166.09 (C=O) ppm; HRMS-ESI m/z [$M-\text{H}$] $^+$ calcd for $\text{C}_{16}\text{H}_{14}\text{ClN}_2\text{O}_2$: 301.07438, found: 301.07494.

4.2.5.7. 2-Chloro-N-[3-(4-methoxy-phenylsulfamoyl)-phenyl]-acetamide (162). Prepared from compound **154** (1.49 g, 5.3 mmol) to yield **162** as light brown powder (0.57 g, 30%) mp: 165–169 °C; ν_{\max} (KBr disc) 3352, 1670, 1593, 1535 cm^{-1} ; $^1\text{H NMR}$ (300 MHz, DMSO- d_6): δ 3.77 (s, 2H), 4.29 (s, 3H), 6.95–7.62 (m, 6H), 7.92 (d, 2H, J 7.2 Hz), 8.16 (s, 1H), 10.74 (s, 1H) ppm; $^{13}\text{C NMR}$ (75 MHz, DMSO- d_6): δ 44.15 (CH_2), 56.23 (CH_3), 115.41 (CH), 118.81 (CH), 123.57 (CH), 125.39 (CH), 126.14 (C), 130.89 ($2 \times \text{CH}$), 133.26 ($2 \times \text{CH}$), 139.86 (C), 139.98 (C), 161.27 (C), 165.95 (C=O) ppm; HRMS-ESI m/z [M] $^+$ calcd for $\text{C}_{15}\text{H}_{15}\text{ClN}_2\text{O}_4\text{S}$: 354.04410, found: 354.26951.

4.2.5.8. 2-Chloro-N-[3-(toluene-4-sulfonylamino)-phenyl]-acetamide (163). Prepared from **155** (13.0 g, 0.049 mol) to yield **163** as light brown powder (14.57 g, 80%) mp 173–176 °C; ν_{\max} (thin film) 3564, 1720, 1543 cm^{-1} ; $^1\text{H NMR}$ (300 MHz, DMSO- d_6): δ 2.06 (s, 3H), 4.23 (s, 2H), 6.61 (d, 1H, J 7.8 Hz), 7.35 (m, 1H), 7.41 (s, 1H), 7.41 (m, 2H), 7.46 (d, 2H, J 8.1 Hz), 7.67 (d, 2H, J 8.1 Hz), 10.49 (s, 1H); $^{13}\text{C NMR}$ (75 MHz, DMSO- d_6): δ 21.88 (CH_3), 44.20 (CH_2), 121.48 (CH), 122.50 (CH), 127.03 (CH), 128.71 ($2 \times \text{CH}$), 130.41 (CH), 130.66 ($2 \times \text{CH}$), 134.67 (C), 136.36 (C), 140.12 (C), 146.19 (C), 165.60 (C=O) ppm.

4.2.6. Synthesis of the pyridinium acetamido-phenylbenzamides and -phenylbenz sulfonamides (164–185)

To magnetically-stirred neat pyridine, nicotinamide or *N*-phenylethyl nicotinamide (**178**) (3.0 equiv) heated to 120–130 °C, the particular *mono*-chloromethyl-acetamido-derivative (**156–163**) was added as neat powder (1.0 equiv). The reaction mixture was stirred at 120–130 °C for 10–15 min then cooled to room temperature. Subsequently, the resulting solid mass was suspended in dry acetone (50 mL) and stirred at room temperature for 1 h. The resulting suspensions were filtered and the solid residues were further washed with acetone (3×100 mL) over 1 h periods to yield the pyridinium derivatives (Scheme 7).

4.2.6.1. 1-[(3-*p*-Tolylcarbamoyl-phenylcarbamoyl)-methyl]-pyridinium chloride (164). Prepared from compound **156** (0.3 g, 1.0 mmol) and pyridine to yield **164** as white powder (0.3 g, 80%) mp: 263–266 °C (Decomp.); ν_{\max} (KBr disc) 3448, 1689, 1670 cm^{-1} ; $^1\text{H NMR}$ (300 MHz, DMSO- d_6): δ 2.24 (s, 3H), 5.7 (s, 2H), 7.11 (d, 2H, J 8.7 Hz), 7.46 (t, 1H), 7.62 (d, 2H, J 8.4 Hz), 7.70 (d, 1H, J 7.8 Hz), 7.82 (d, 1H, J 7.8 Hz), 8.18 (m, 3H), 8.70 (t, 1H), 9.12 (d, 2H, J 6 Hz), 10.26 (s, 1H), 11.52 (s, 1H) ppm; $^{13}\text{C NMR}$ (75 MHz, DMSO- d_6): δ 21.18 (CH_3), 62.82 (CH_2), 119.44 (CH), 121.08 ($2 \times \text{CH}$), 122.68 (CH), 123.47 (CH), 128.21 (CH), 129.57 ($2 \times \text{CH}$), 129.65 ($2 \times \text{CH}$), 133.31 (C), 136.63 (C), 137.26 (C), 139.23 (C), 146.93 (CH), 147.14 ($2 \times \text{CH}$), 164.25 (C=O), 165.79 (C=O) ppm; HRMS-ESI m/z [M] $^+$ calcd for $\text{C}_{21}\text{H}_{20}\text{N}_3\text{O}_2$: 346.15555, found: 346.15500.

4.2.6.2. 1-[(3-*m*-Tolylcarbamoyl-phenylcarbamoyl)-methyl]-pyridinium chloride (165). Prepared from compound **157** (0.3 g, 1.0 mmol) and pyridine to yield **165** as white powder (0.28 g, 80%) mp: 271 °C (Decomp.); ν_{\max} (KBr disc) 3448, 3352, 1701, 1654, 1539 cm^{-1} ; $^1\text{H NMR}$ (300 MHz, DMSO- d_6): δ 2.27 (s, 3H), 5.74 (s, 2H), 6.90 (d, 1H, J Hz), 7.19 (t, 1H), 7.75 (m, 3H), 7.69 (d, 1H, J 7.8), 7.82 (d, 1H, J 7.8 Hz), 8.14 (s, 1H), 8.21 (t, 2H), 8.68 (t, 1H), 9.09 (d, 2H, J 6 Hz), 10.23 (s, 1H), 11.35 (s, 1H) ppm; $^{13}\text{C NMR}$ (75 MHz, DMSO- d_6): δ 21.89 (CH_3), 62.84 (CH_2), 118.29 (CH), 119.52 (CH), 121.63 (CH), 122.78 (CH), 123.50 (CH), 125.11 (CH), 128.23 ($2 \times \text{CH}$), 129.11 (CH), 129.64 (CH), 136.56 (C), 138.41 (C), 139.14 (C), 139.67 (C), 146.98 ($2 \times \text{CH}$), 147.14 (CH), 164.20 (C=O), 165.86 (C=O) ppm; HRMS-ESI m/z [M] $^+$ calcd for $\text{C}_{21}\text{H}_{20}\text{N}_3\text{O}_2$: 346.15555, found: 346.15500.

4.2.6.3. 1-[[3-(4-Chloro-phenylcarbamoyl)-phenylcarbamoyl]-methyl]-pyridinium chloride (166). Prepared from **158** (0.3 g, 1.0 mmol) and pyridine to yield **166** as white powder (0.19 g, 55.5%) mp: 266–269 °C (Decomp.); ν_{\max} (KBr disc) 3448, 3294, 1689, 1651 cm^{-1} ; $^1\text{H NMR}$ (300 MHz, DMSO- d_6): δ 5.76 (s, 2H), 7.37 (d, 2H, J 8.7 Hz), 7.48 (t, 1H), 7.72 (dd, 1H, J 0.9, 7.5 Hz), 7.81 (d, 2H, J 6.6 Hz), 7.83 (s, 1H), 8.17 (d, 1H, J 4.8 Hz), 8.22 (d, 2H, J 6.6 Hz), 8.67 (t, 1H), 9.10 (d, 2H, J 6.6 Hz), 10.48 (s, 1H), 11.41 (s, 1H) ppm; $^{13}\text{C NMR}$ (75 MHz, DMSO- d_6): δ 62.82 (CH_2), 119.46 (CH), 122.56 ($2 \times \text{CH}$), 122.92 (CH), 123.57 (CH), 127.97 (C), 128.22 ($2 \times \text{CH}$), 129.20 ($2 \times \text{CH}$), 129.69 (CH), 136.26 (C), 138.77 (C), 139.26 (C), 146.96 ($2 \times \text{CH}$), 147.15 (CH), 164.28 (C=O), 166.06 (C=O) ppm; HRMS-ESI m/z [M] $^+$ calcd for $\text{C}_{20}\text{H}_{17}\text{ClN}_3\text{O}_2$: 366.10093, found: 366.10038.

4.2.6.4. 1-[[3-(4-Methoxy-phenylcarbamoyl)-phenylcarbamoyl]-methyl]-pyridinium chloride (167). Prepared from compound **159** (0.2 g, 0.6 mmol) and pyridine to yield **167** as Off-white powder (0.2 g, 85%) mp: 245–246 °C (Decomp.); ν_{\max} (KBr disc) 3406, 1685, 1620 cm^{-1} ; $^1\text{H NMR}$ (300 MHz, DMSO- d_6): δ 3.71 (s, 2H), 5.74 (s, 2H), 6.90 (dd, 2H, J 3, 9 Hz), 7.47 (t, 1H), 7.64 (dd, 2H, J 3, 6 Hz), 7.70 (d, 1H, J 8.1 Hz), 7.80 (dd, 1H, J 7.8, 1.2 Hz), 8.14 (s, 1H), 8.21 (dd, 2H, J 6.6, 7.8 Hz), 8.65 (t, 1H), 9.08 (d, 2H, J 5.4 Hz), 10.19 (s, 1H), 11.32 (s, 1H) ppm; $^{13}\text{C NMR}$ (75 MHz, DMSO- d_6): δ 55.85 (CH_3), 62.81 (CH_2), 114.40 ($2 \times \text{CH}$), 119.43 (CH), 122.61 ($2 \times \text{CH}$), 122.68 (CH), 123.40 (CH), 128.23 ($2 \times \text{CH}$), 129.62 (CH), 132.80 (C), 136.64 (C), 139.16 (C), 146.96 (CH), 147.15 ($2 \times \text{CH}$), 156.23 (C), 164.23 (C=O), 165.49 (C=O) ppm; HRMS-ESI m/z [M] $^+$ calcd for $\text{C}_{21}\text{H}_{20}\text{N}_3\text{O}_3$: 363.15382, found: 363.15328.

4.2.6.5. 1-[(3-Benzoylamino-phenylcarbamoyl)-methyl]-pyridinium chloride (168). Prepared from **160** (0.286 g, 0.99 mmol) and pyridine to yield **168** (0.3 g, 88%) mp: 238–239 °C (Decomp.); ν_{\max} (thin film) 3444, 1730, 1543 cm^{-1} ; $^1\text{H NMR}$ (300 MHz, DMSO- d_6): δ 5.75 (s, 2H), 7.25–7.56 (m, 7H), 7.95 (d, 2H, J 7.2 Hz), 8.21 (t, 2H), 8.67 (t, 1H), 9.11 (d, 2H, J 6 Hz), 10.38 (s, 1H), 11.22 (s, 1H) ppm; $^{13}\text{C NMR}$ (75 MHz, DMSO- d_6): δ 62.87 (CH_2), 112.16 (CH), 115.30 (CH), 116.79 (CH), 128.18 (CH), 128.43 ($2 \times \text{CH}$), 129.03 ($2 \times \text{CH}$), 129.60 (CH), 132.3 (CH), 135.30 (CH), 139.18 (CH), 140.35 (CH), 146.88 ($2 \times \text{CH}$), 147.13 ($2 \times \text{CH}$), 163.94 (C=O), 166.27 (C=O) ppm; HRMS-ESI m/z [M] $^+$ calcd for $\text{C}_{20}\text{H}_{18}\text{N}_3\text{O}_2$: 332.13990, found: 332.13935.

4.2.6.6. 1[[3-(4-Methyl-benzoylamino)-phenylcarbamoyl]-methyl]-pyridinium chloride (169). Prepared from **161** (0.283 g, 0.93 mmol) and pyridine to yield **169** (0.31 g, 89%) mp: 262–265 °C (Decomp.); ν_{\max} (thin film) 3614, 1654, 1539 cm^{-1} ; $^1\text{H NMR}$ (300 MHz, DMSO- d_6): δ 2.37 (s, 3H), 5.70 (s, 2H), 7.28–7.44 (m, 7H), 7.86 (d, 2H, J 7.8 Hz), 8.22 (t, 2H), 8.67 (t, 1H), 9.08 (d, 1H, J 6 Hz), 10.25 (s, 1H), 11.02 (s, 1H) ppm; $^{13}\text{C NMR}$ (75 MHz, DMSO- d_6): δ 21.72 (CH_3), 62.86 (CH_2), 112.04 (CH), 115.12 (CH), 116.72 (CH), 128.19 ($2 \times \text{CH}$), 128.44 ($2 \times \text{CH}$), 129.58 (CH), 129.65 ($2 \times \text{CH}$), 132.60 (C), 139.11 (C), 140.46 (C), 142.33 (C), 146.91 (CH), 147.15 ($2 \times \text{CH}$), 163.92 (C=O), 166.09 (C=O) ppm; HRMS-ESI m/z [M] $^+$ calcd for $\text{C}_{21}\text{H}_{20}\text{N}_3\text{O}_2$: 346.15555, found: 346.15500.

4.2.6.7. 1-[[3-(4-Methoxy-phenylsulfamoyl)-phenylcarbamoyl]-methyl]-pyridinium chloride (170). Prepared from compound **162** (0.1 g, 0.3 mmol) and pyridine to yield **170** as light brown powder (0.11 g, 98%) mp 209 °C (Decomp.); ν_{\max} (KBr disc) 3421, 1701, 1635 cm^{-1} ; $^1\text{H NMR}$ (300 MHz, DMSO- d_6): δ 3.76 (s, 3H), 5.77 (s, 2H), 6.93 (s, 1H), 7.50 (d, 2H, J 8.1 Hz), 7.65 (m, 3H), 7.97 (d, 2H, J 8.4 Hz), 8.24 (m, 3H), 8.71 (t, 1H), 9.10 (d, 2H, J 5.4 Hz), 11.61 (s, 1H) ppm; $^{13}\text{C NMR}$ (75 MHz, DMSO- d_6): δ 56.20 (CH_3), 62.79 (CH_2), 115.36 ($2 \times \text{CH}$), 118.64 ($2 \times \text{CH}$), 123.68

(CH), 125.23 (CH), 126.04 (C), 128.21 (2 × CH), 131.01 (CH), 133.18 (CH), 139.75 (C), 139.94 (C), 147.02 (CH), 147.15 (2 × CH), 161.18 (C), 164.68 (C=O) ppm; HRMS-ESI m/z $[M-H]^+$ calcd for $C_{20}H_{19}N_3O_4S$: 397.10963, found: 397.10908.

4.2.6.8. 3-Carbamoyl-1-[(3-*p*-tolylcarbamoyl-phenylcarbamoyl)-methyl]-pyridinium chloride (171). Prepared from compound **156** (0.3 g, 0.99 mmol) and nicotinamide to yield **171** as white powder (0.35 g, 83%) mp: 287–290 °C (Decomp.); ν_{\max} (KBr disc) 3298, 1689, 1651 cm^{-1} ; 1H NMR (300 MHz, DMSO- d_6): δ 2.24 (s, 3H), 5.81 (s, 2H), 7.11 (d, 2H, J 7.8 Hz), 7.46 (t, 1H), 7.61 (d, 2H, J 7.8 Hz), 7.69 (d, 1H, J 7.8 Hz), 7.80 (d, 1H, J 7.8 Hz), 8.16 (d, 2H, J 12 Hz), 8.32 (t, 1H), 8.77 (s, 1H), 9.09 (d, 1H, J 7.8 Hz), 9.21 (d, 1H, J 5.7 Hz), 9.62 (s, 1H), 10.24 (s, 1H), 11.39 (s, 1H) ppm; ^{13}C NMR (75 MHz, DMSO- d_6): δ 21.19 (CH₃), 63.06 (CH₂), 119.4 (CH), 121.09 (2 × CH), 122.70 (CH), 123.51 (CH), 127.91 (CH), 129.66 (3 × CH), 133.32 (C), 133.89 (C), 136.64 (C), 137.25 (C), 139.16 (C), 144.80 (CH), 147.40 (CH), 148.74 (CH), 163.43 (C=O), 164.04 (C=O), 165.74 (C=O) ppm; HRMS-ESI m/z $[M]^+$ calcd for $C_{22}H_{21}N_4O_3$: 390.16472, found: 390.16411.

4.2.6.9. 3-Carbamoyl-1-[(3-*m*-tolylcarbamoyl-phenylcarbamoyl)-methyl]-pyridinium chloride (172). Prepared from compound **157** (0.3 g, 1.0 mmol) and nicotinamide to yield **172** as Off-white powder (0.14 g, 33%) mp: 242–244 °C (Decomp.); ν_{\max} (KBr disc) 3298, 1685, 1651 cm^{-1} ; 1H NMR (300 MHz, DMSO- d_6): δ 2.27 (s, 3H), 5.79 (s, 2H), 6.88 (d, 1H, J 7.2 Hz), 7.19 (t, 1H), 7.46 (t, 1H), 7.52 (d, 1H, J 9), 7.58 (s, 1H), 7.69 (d, 1H, J 8.1 Hz), 7.81 (dd, 1H, J 1.2, 6.9 Hz), 8.13 (s, 1H), 8.19 (s, 1H), 8.32 (t, 1H), 8.73 (s, 1H), 9.07 (d, 1H, J 8.1 Hz), 9.20 (d, 1H, J 6 Hz), 9.6 (s, 1H), 10.23 (s, 1H), 11.30 (s, 1H) ppm; ^{13}C NMR (75 MHz, DMSO- d_6): δ 21.9 (CH₃), 63.03 (CH₂), 118.26 (CH), 119.46 (CH), 121.60 (CH), 122.74 (CH), 123.55 (CH), 125.11 (CH), 127.91 (CH), 129.13 (CH), 129.67 (CH), 133.93 (C), 136.63 (C), 138.42 (C), 139.15 (C), 139.68 (C), 144.76 (CH), 147.43 (CH), 148.75 (CH), 163.46 (C=O), 164.07 (C=O), 165.87 (C=O) ppm; HRMS-ESI m/z $[M]^+$ calcd for $C_{22}H_{21}N_4O_3$: 390.16472, found: 390.16411.

4.2.6.10. 3-Carbamoyl-1-[(3-(4-chloro-phenylcarbamoyl)-phenylcarbamoyl)-methyl]-pyridinium chloride (173). Prepared from compound **158** (0.3 g, 1.0 mmol) and nicotinamide as white powder (0.168 g, 44%) mp: 294–296 °C (Decomp.); ν_{\max} (KBr disc) 3282, 1693, 1651 cm^{-1} ; 1H NMR (300 MHz, DMSO- d_6): δ 5.78 (s, 2H), 7.36 (d, 2H, J 8.7 Hz), 7.49 (t, 1H), 7.71 (d, 1H, J 7.2 Hz), 7.79 (d, 3H, J 8.7 Hz), 8.16 (d, 2H, J 12 Hz), 8.32 (t, 1H), 8.71 (s, 1H), 9.07 (d, 1H, J 8.4 Hz), 9.19 (d, 1H, J 6.3 Hz), 9.58 (s, 1H), 10.46 (s, 1H), 11.28 (s, 1H) ppm; ^{13}C NMR (75 MHz, DMSO- d_6): δ 63.02 (CH₂), 119.47 (CH), 122.55 (2 × CH), 122.92 (CH), 123.61 (CH), 127.91 (CH), 129.20 (2 × CH), 129.74 (CH), 129.75 (C), 133.91 (C), 136.27 (C), 138.75 (C), 139.19 (C), 144.74 (CH), 147.42 (CH), 148.74 (CH), 163.45 (C=O), 164.08 (C=O), 166.02 (C=O) ppm; HRMS-ESI m/z $[M]^+$ calcd for $C_{21}H_{18}ClN_4O_3$: requires 409.10674, found: 409.10619.

4.2.6.11. 3-Carbamoyl-1-[(3-(4-methoxy-phenylcarbamoyl)-phenylcarbamoyl)-methyl]-pyridinium chloride (174). Prepared from compound **159** (0.2 g, 0.6 mmol) and nicotinamide to yield **174** as light brown powder (0.23 g, 87%) mp: 255–257 °C (Decomp.); ν_{\max} (KBr disc) 3298, 1685, 1647 cm^{-1} ; 1H NMR (300 MHz, DMSO- d_6): δ 3.74 (s, 3H), 5.79 (s, 2H), 6.89 (d, 2H, J 9 Hz), 7.96 (t, 1H), 7.65 (d, 2H, J 8.7 Hz), 7.71 (d, 2H, J 9), 7.80 (d, 1H, J 9 Hz), 8.16 (d, 2H, J 9 Hz), 8.34 (t, 1H), 8.69 (s, 1H), 9.08 (d, 1H, J 9 Hz), 9.20 (d, 1H, J 6 Hz), 9.59 (s, 1H), 10.17 (s, 1H), 11.19 (s, 1H) ppm; ^{13}C NMR (75 MHz, DMSO- d_6): δ 55.85 (CH₃), 63.03 (CH₂), 114.4 (2 × CH), 119.47 (CH), 122.68 (2 × CH),

123.41 (CH), 127.90 (CH), 129.61 (2 × CH), 132.79 (C), 133.96 (C), 136.66 (C), 139.08 (C), 144.71 (CH), 147.40 (CH), 148.72 (CH), 156.25 (C), 163.43 (C=O), 163.99 (C=O), 165.44 (C=O) ppm; HRMS-ESI m/z $[M]^+$ calcd for $C_{22}H_{21}N_4O_4$: 406.15964, found: 406.15909.

4.2.6.12. 1-[(3-Benzoylamino-phenylcarbamoyl)-methyl]3-carbamoyl-pyridinium chloride (175). Prepared from **160** (0.5 g, 1.48 mmol) and nicotinamide to yield (0.17 g, 49%) mp: 286–288 °C (Decomp.); ν_{\max} (thin film) 3564, 1732, 1508 cm^{-1} ; 1H NMR (300 MHz, DMSO- d_6): δ 5.77 (s, 2H), 7.29–7.60 (m, 7H), 7.95 (d, 1H, J 8.4 Hz), 8.31 (d, 1H, J 7.5 Hz), 8.33 (t, 1H), 8.76 (s, 2H), 9.10 (d, 1H, J 8.1 Hz), 9.21 (d, 1H, J 6 Hz), 9.61 (s, 1H), 10.36 (s, 1H), 11.07 (s, 1H) ppm; ^{13}C NMR (75 MHz, DMSO- d_6): δ 63.09 (CH₂), 112.05 (CH), 115.24 (CH), 116.74 (CH), 127.87 (CH), 128.42 (2 × CH), 129.05 (2 × CH), 129.68 (CH), 132.32 (CH), 133.87 (C), 135.51 (C), 139.13 (C), 140.38 (C), 144.71 (CH), 147.44 (CH), 148.44 (CH), 163.47 (C=O), 166.30 (C=O), 175.63 (C=O) ppm; HRMS-ESI m/z $[M]^+$ calcd for $C_{21}H_{19}N_4O_3$: 375.14572, found: 375.14517.

4.2.6.13. 3-Carbamoyl-1-[(3-(4-methyl-benzoylamino)-phenylcarbamoyl)-methyl]-pyridinium chloride (176). Prepared from **161** (0.25 g, 0.87 mmol) and nicotinamide to yield (0.22 g, 64%) mp: 289 °C (Decomp.); ν_{\max} (thin film) 3730, 1680, 1539 cm^{-1} ; 1H NMR (300 MHz, DMSO- d_6): δ 2.47 (s, 3H), 5.77 (s, 2H), 7.23–7.46 (m, 5H), 7.86 (d, 2H, J 8.4 Hz), 8.20 (t, 1H), 8.31 (dd, 1H, J 2.1, 6 Hz), 8.78 (s, 2H), 9.11 (d, 1H, J 8.4 Hz), 9.21 (d, 1H, J 6 Hz), 9.62 (s, 1H), 10.27 (s, 1H), 11.12 (s, 1H) ppm; ^{13}C NMR (75 MHz, DMSO- d_6): δ 21.7 (CH₃), 63.08 (CH₂), 112.12 (CH), 115.16 (CH), 116.76 (CH), 127.85 (CH), 128.46 (2C), 129.54 (3 × CH), 132.58 (C), 133.83 (C), 139.10 (C), 140.44 (C), 142.30 (C), 144.72 (CH), 147.41 (CH), 148.72 (CH), 163.44 (C=O), 163.71 (C=O), 166.07 (C=O) ppm; HRMS-ESI m/z $[M]^+$ calcd for $C_{22}H_{21}N_4O_3$: 390.16472, found: 390.16411.

4.2.6.14. 3-Carbamoyl-1-[(3-(4-methoxy-phenylsulfamoyl)-phenylcarbamoyl)-methyl]-pyridinium chloride (177). Prepared from compound **162** (0.122 g, 3.4 mmol) and nicotinamide to yield **177** (0.10 g, 64%) mp: 210–212 °C (Decomp.); ν_{\max} (KBr disc) 3406, 1689, 1600 cm^{-1} ; 1H NMR (300 MHz, DMSO- d_6): δ 3.76 (s, 3H), 5.82 (s, 2H), 6.94 (s, 1H), 7.51 (d, 2H, J 7.8 Hz), 7.65 (m, 3H), 7.96 (d, 2H, J 8.4 Hz), 8.19 (s, 1H), 8.26 (s, 1H), 8.35 (t, 1H), 8.72 (s, 1H), 9.10 (d, 1H, J 7.8 Hz), 9.22 (d, 1H, J 5.7 Hz), 9.61 (s, 1H), 11.64 (s, 1H) ppm; ^{13}C NMR (75 MHz, DMSO- d_6): δ 56.20 (CH₃), 63.04 (CH₂), 115.39 (2 × CH), 118.67 (2 × CH), 123.72 (CH), 125.28 (CH), 126.07 (C), 127.91 (CH), 131.01 (CH), 132.01 (C), 133.95 (CH), 139.75 (C), 139.96 (C), 144.80 (CH), 147.46 (CH), 148.74 (CH), 151.74 (C), 163.43 (C=O), 164.50 (C=O) ppm; HRMS-ESI m/z $[M-H]^+$ calcd for $C_{21}H_{20}N_4O_5S$: 441.11880, found: 441.11825.

4.2.6.15. 3-Carbamoyl-1-[(3-(toluene-4-sulfonylamino)-phenylcarbamoyl)-methyl]-pyridinium chloride (178). Prepared from **163** (0.5 g, 1.4 mmol) and nicotinamide to yield **178** as white powder (0.46 g, 68%) mp: 260 °C (Decomp.); ν_{\max} (thin film) 3614, 1700, 1539, 1219 cm^{-1} ; 1H NMR (300 MHz, DMSO- d_6): δ 2.31 (s, 3H), 5.76 (s, D₂O exchangeable, 2H), 6.63 (d, 1H, J 8.1 Hz), 7.34–7.65 (m, 10H), 8.21 (s, 1H), 8.34 (t, 1H), 8.67 (s, 1H), 9.1 (dd, 2H, J 20.1, 7.8 Hz), 9.53 (s, 1H), 11.11 (s, 1H); ^{13}C NMR (75 MHz, DMSO- d_6): δ 21.86 (CH₃), 63.024 (CH₂), 121.39 (CH), 122.577 (CH), 127.09 (CH), 127.91 (CH), 128.72 (2 × CH), 130.53 (CH), 130.69 (2 × CH), 133.90 (C), 134.76 (C), 136.33 (C), 139.92 (C), 144.74 (CH), 146.18 (C), 147.511 (CH), 148.78 (CH), 163.46 (C=O), 164.16 (C=O) ppm; HRMS-ESI m/z $[M]^+$ calcd for

C₂₁H₂₁N₄O₄S: 426.13171, found: 426.13116; Anal. Calcd for C₂₁H₂₁ClN₄O₄S: C, 54.72; H, 4.59. Found: C, 54.50; H, 4.43.

4.2.6.16. 3-Phenethylcarbamoyl-1-[(3-*p*-tolylcarbamoyl-phenylcarbamoyl)-methyl]-pyridinium chloride (179). Prepared from compound **156** (0.3 g, 0.99 mmol) and **186** as white powder (0.36 g, 68%) mp: 231–234 °C (Decomp.); ν_{\max} (KBr disc) 3290, 1693, 1647 cm⁻¹; ¹H NMR (300 MHz, DMSO-*d*₆): δ 2.25 (s, 3H), 2.88 (t, 2H), 3.56 (t, 2H), 5.7 (s, 2H), 7.13 (d, 2H, *J* 8.4 Hz), 7.2 (dd, 1H, *J* 1.5, 7.2 Hz), 7.26 (m, 4H), 7.47 (t, 1H), 7.62 (d, 2H, *J* 8.1 Hz), 7.70 (d, 1H, *J* 7.8 Hz), 7.80 (d, 1H, *J* 8.1 Hz), 8.14 (s, 1H), 8.32 (t, 1H), 9.06 (d, 1H, *J* 8.4 Hz), 9.20 (d, *J* 6 Hz, 1H), 9.52 (s, 1H), 9.58 (s, 1H), 10.23 (s, 1H), 11.32 (s, 1H) ppm; ¹³C NMR (75 MHz, DMSO-*d*₆): δ 21.19 (CH₃), 35.38 (CH₂), 41.85 (CH₂), 63.05 (CH₂), 119.46 (CH), 121.07 (2 × CH), 122.68 (CH), 123.50 (CH), 126.94 (CH), 127.91 (CH), 129.09 (2 × CH), 129.36 (2 × CH), 129.67 (2 × CH), 133.34 (C), 133.96 (C), 136.66 (C), 137.24 (C), 139.15 (C), 139.78 (C), 140.89 (CH), 144.46 (CH), 147.16 (CH), 148.71 (CH), 161.78 (C=O), 164.04 (C=O), 165.72 (C=O) ppm; HRMS-ESI *m/z* [M]⁺ calcd for C₃₀H₂₉N₄O₃: 493.22397, found: 493.22342; Anal. Calcd for C₃₀H₂₉ClN₄O₃: C, 68.11; H, 5.53. Found: C, 67.80; H, 5.13.

4.2.6.17. 3-Phenethylcarbamoyl-1-[(3-*m*-tolylcarbamoyl-phenylcarbamoyl)-methyl]-pyridinium chloride (180). Prepared from compound **157** (0.3 g, 0.1 mmol) and **186** as white powder (0.37 g, 70%) mp: 206–209 °C (Decomp.); ν_{\max} (KBr disc) 3294, 1689, 1662 cm⁻¹; ¹H NMR (300 MHz, DMSO-*d*₆): δ 2.27 (s, 3H), 2.85 (t, 2H), 3.54 (t, 2H), 5.80 (s, 2H), 6.89 (d, 1H, *J* 7.2 Hz), 7.22 (m, 5H), 7.55 (m, 4H), 7.70 (d, 1H, *J* 7.2 Hz), 7.81 (d, 1H, *J* 7.5 Hz), 8.1 (s, 1H), 8.32 (t, 1H), 9.07 (d, 1H, *J* 6.9 Hz), 9.20 (d, 1H, *J* 6.3 Hz), 9.54 (t, 1H), 9.58 (s, 1H), 10.23 (s, 1H), 11.35 (s, 1H) ppm; ¹³C NMR (75 MHz, DMSO-*d*₆): δ 21.91 (CH₃), 35.38 (CH₂), 41.84 (CH₂), 63.08 (CH₂), 118.27 (CH), 119.48 (CH), 121.60 (CH), 122.76 (CH), 123.56 (CH), 125.10 (CH), 126.94 (CH), 127.92 (CH), 129.06 (2 × CH), 129.12 (CH), 129.36 (2 × CH), 129.67 (CH), 133.95 (C), 136.64 (C), 138.41 (C), 139.17 (C), 139.69 (C), 139.79 (C), 144.49 (CH), 147.18 (CH), 148.71 (CH), 161.75 (C=O), 164.05 (C=O), 165.89 (C=O) ppm; HRMS-ESI *m/z* [M]⁺ calcd for C₃₀H₂₉N₄O₃: 493.22397, found: 493.22342; Anal. Calcd for C₃₀H₂₉ClN₄O₃: C, 68.11; H, 5.53. Found: C, 68.35; H, 5.64.

4.2.6.18. 1-[[3-(4-Chloro-phenylcarbamoyl)-phenylcarbamoyl]-methyl]-3-phenethylcarbamoyl-pyridinium chloride (181). Prepared from compound **158** (0.3 g, 1 mmol) and **186** as white powder (0.262 g, 56%) mp: 240–242 °C (Decomp.); ν_{\max} (KBr disc) 3421, 1689, 1662, 1593 cm⁻¹; ¹H NMR (300 MHz, DMSO-*d*₆): δ 2.87 (t, 2H), 3.55 (t, 2H), 5.81 (s, 2H), 7.18–7.81 (m, 12H), 8.17 (s, 1H), 8.32 (t, 1H), 9.09 (d, 1H, *J* 7.8 Hz), 9.21 (d, 1H, *J* 6 Hz), 9.58 (s, 2H), 10.49 (s, 1H), 11.42 (s, 1H) ppm; ¹³C NMR (75 MHz, DMSO-*d*₆): δ 35.38 (CH₂), 41.84 (CH₂), 63.07 (CH₂), 119.49 (CH), 122.57 (2 × CH), 122.94 (CH), 123.64 (CH), 126.92 (CH), 127.19 (2 × CH), 127.96 (C), 129.08 (2 × CH), 129.19 (2 × CH), 129.35 (CH), 129.69 (CH), 133.93 (C), 136.25 (C), 138.79 (C), 139.22 (C), 139.79 (C), 144.49 (CH), 147.15 (CH), 148.69 (CH), 161.75 (C=O), 164.07 (C=O), 166.05 (C=O) ppm; HRMS-ESI *m/z* [M]⁺ calcd for C₂₉H₂₆ClN₄O₃: 513.16934, found: 513.16879.

4.2.6.19. 1-[[3-(4-Methoxy-phenylcarbamoyl)-phenylcarbamoyl]-methyl]-3-phenethylcarbamoyl-pyridinium chloride (182). Prepared from compound **159** (0.2 g, 0.6 mmol) and **186** to yield **182** as light yellow powder (0.18 g, 55%) mp: 222–225 °C (Decomp.); ν_{\max} 3282, 1662, 1593, 1512 (KBr disc) cm⁻¹; ¹H NMR (300 MHz, DMSO-*d*₆): δ 2.88 (t, 2H), 3.52 (t, 2H), 3.69 (s, 3H), 5.75 (s, 2H), 6.87 (d, 2H, *J* 8.7 Hz), 7.16–7.78 (m, 10H), 8.11 (s, 1H), 8.30 (t, 1H), 9.02 (d, 1H, *J* 7.5 Hz), 9.16 (d, 1H, *J* 5.4 Hz), 9.42 (s, 1H), 9.53 (s, 1H), 10.13 (s, 1H), 11.19 (s, 1H) ppm; ¹³C NMR

(75 MHz, DMSO-*d*₆): δ 35.37 (CH₃), 41.84 (CH₂), 55.85 (CH₂), 63.07 (CH₂), 114.37 (2 × CH), 119.45 (CH), 122.68 (3 × CH), 123.48 (CH), 126.92 (CH), 127.90 (CH), 129.08 (2 × CH), 129.35 (2 × CH), 129.58 (CH), 132.84 (C), 133.92 (C), 136.64 (C), 139.18 (C), 139.81 (C), 144.52 (CH), 147.15 (CH), 148.69 (CH), 156.21 (C), 161.74 (C=O), 164.03 (C=O), 165.52 (C=O) ppm; HRMS-ESI *m/z* [M]⁺ calcd for C₃₀H₂₉N₄O₄: 509.21888, found: 509.21833.

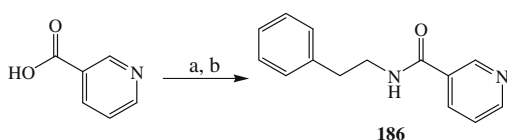
4.2.6.20. 1-[[3-(Benzoylamino-phenylcarbamoyl)-methyl]-3-phenethylcarbamoyl-pyridinium chloride (183). Prepared from **160** (0.3 g, 1 mmol) and **186** to yield **183** (0.47 g, 92%) mp: 204 °C (Decomp.); ν_{\max} (KBr disc) 3448, 1705, 1662, 1543 cm⁻¹; ¹H NMR (300 MHz, DMSO-*d*₆): δ 2.88 (t, 2H), 3.56 (t, 2H), 5.77 (s, 2H), 7.15–7.58 (m, 12H), 7.94 (d, 2H, *J* 7.8 Hz), 8.22 (s, 1H), 8.31 (t, 1H), 9.10 (d, 1H, *J* 8.1 Hz), 9.20 (d, 1H, *J* 5.7 Hz), 9.5 (s, 1H), 10.36 (s, 1H), 11.11 (s, 1H) ppm; ¹³C NMR (75 MHz, DMSO-*d*₆): δ 35.38 (CH₂), 41.84 (CH₂), 63.11 (CH₂), 112.12 (CH), 115.28 (CH), 116.78 (CH), 126.92 (CH), 127.86 (CH), 128.41 (2 × CH), 129.03 (2 × CH), 129.09 (2 × CH), 129.35 (2 × CH), 129.64 (CH), 132.30 (CH), 133.89 (C), 135.50 (C), 139.13 (C), 139.13 (C), 139.81 (C), 140.38 (C), 144.44 (CH), 147.16 (CH), 148.68 (CH), 161.76 (C=O), 163.72 (C=O), 166.28 (C=O) ppm; HRMS-ESI *m/z* [M]⁺ calcd for C₂₉H₂₇N₄O₃: 479.20832, found: 479.20777.

4.2.6.21. 1-[[3-(4-Methyl-benzoylamino)-phenylcarbamoyl]-methyl]-3-phenethylcarbamoyl-pyridinium chloride (184). This compound was prepared from **161** (0.3 g, 1.0 mmol) and **186**. (0.31 g, 59%) mp: 225 °C (Decomp.); ν_{\max} (KBr disc) 3309, 1689, 1666, 1608, 1562 cm⁻¹; ¹H NMR (300 MHz, DMSO-*d*₆): δ 2.35 (s, 3H), 2.88 (t, 2H), 3.53 (t, 2H), 5.78 (2, 2H), 7.18–7.47 (m, 9H), 7.86 (d, 2H, *J* 7.5 Hz), 8.22 (s, 1H), 8.31 (t, 1H), 9.11 (d, 1H, *J* 7.5 Hz), 9.20 (d, 1H, *J* 5.4 Hz), 9.62 (t, 2H), 9.65 (s, 1H), 10.27 (s, 1H), 11.14 (s, 1H) ppm; ¹³C NMR (75 MHz, DMSO-*d*₆): δ 21.70 (CH₃), 35.38 (CH₂), 41.84 (CH₂), 63.10 (CH₂), 112.16 (CH), 115.19 (CH), 116.8 (CH), 126.92 (CH), 127.85 (CH), 128.46 (2 × CH), 129.08 (2 × CH), 129.35 (2 × CH), 129.54 (3 × CH), 132.60 (C), 133.88 (C), 139.11 (C), 139.81 (C), 140.44 (C), 142.29 (C), 144.47 (CH), 147.15 (CH), 148.67 (CH), 161.75 (C=O), 163.70 (C=O), 166.07 (C=O) ppm; HRMS-ESI *m/z* [M+H]⁺ calcd for C₃₀H₃₀N₄O₃: 494.23179, found: 494.26384.

4.2.6.22. 3-Phenethylcarbamoyl-1-[[3-(toluene-4-sulfonylamino)-phenylcarbamoyl]-methyl]-pyridinium chloride (185). Prepared from **163** (0.32 g, 0.9 mmol) and **186** to yield **185** (0.26 g, 50%) mp: 204 °C (Decomp.); ν_{\max} (KBr disc) 3421, 1697, 1666, 1600, 1543 cm⁻¹; ¹H NMR (300 MHz, DMSO-*d*₆): δ 2.39 (s, 3H), 2.88 (t, 2H), 3.55 (t, 2H), 5.75 (s, 2H), 6.61 (d, 1H, *J* 8.1 Hz), 7.19–7.70 (m, 12H), 8.33 (t, 1H), 9.08 (d, 2H, *J* 7.8 Hz), 9.17 (d, 1H, *J* 5.7 Hz), 9.53 (s, 1H), 9.56 (s, 1H), 11.36 (s, 1H) ppm; ¹³C NMR (75 MHz, DMSO-*d*₆): δ 21.83 (CH₃), 35.40 (CH₂), 41.84 (CH₂), 63.29 (CH₂), 121.36 (CH), 122.59 (CH), 126.92 (CH), 127.09 (CH), 127.88 (CH), 128.68 (2 × CH), 129.09 (2 × CH), 129.34 (2 × CH), 130.49 (CH), 130.64 (2 × CH), 134.00 (C), 134.77 (C), 136.35 (C), 139.75 (C), 139.82 (C), 144.38 (CH) 146.13 (C), 147.22 (CH), 148.71 (CH), 161.80 (C=O), 164.09 (C=O) ppm; HRMS-ESI *m/z* [M]⁺ calcd for C₂₉H₂₉N₄O₄S 529.19095, found: 529.19040.

4.2.7. Synthesis of *N*-phenethyl-nicotinamide (186)

Excess oxalyl chloride (99%) was added to nicotinic acid (15 g, 0.12 mol) to form slurry. The mixture was left to dry in the fume hood. Subsequently, neat phenylethylamine (10 mL) was added to the resulting powder in ice bath. The reaction was subsequently warmed to room temperature and stirred for 15 min. Then it was terminated by quenching with 5% aqueous NaHCO₃ solution (300 ml). The resulting crude precipitate was collected and recrystallized from acetone/water (Scheme 8).



Scheme 8. Synthesis of **186**. (a) Oxalyl chloride, (b) quench with 2-phenylethylamine.

4.2.7.1. N-Phenethyl-nicotinamide (186). Yellow crystalline needles (8.12 g, 29%) mp: 58–59 °C; ν_{\max} (KBr disc) 3325, 1635 cm^{-1} ; ^1H NMR (300 MHz, $\text{DMSO-}d_6$): δ 2.83 (t, 2H), 3.51 (t, 2H), 7.15–7.30 (m, 5H), 7.48 (t, 1H), 8.12 (d, 1H, J 7.8 Hz), 8.67 (d, 1H, J 3.6 Hz), 8.76 (s, 1H), 8.94 (s, 1H) ppm; ^{13}C NMR (75 MHz, $\text{DMSO-}d_6$): δ 35.67 (CH_2), 41.55 (CH_2), 124.14 (CH), 126.83 (CH), 129.04 ($2 \times \text{CH}$), 129.36 ($2 \times \text{CH}$), 130.70 (C), 135.54 (CH), 140.06 (C), 148.96 (CH), 152.45 (CH), 165.39 (C=O) ppm; HRMS-ESI m/z [$M+H$] $^+$ calcd for $\text{C}_{14}\text{H}_{15}\text{N}_2\text{O}$: 228.12179, found 228.12124.

4.3. Quantification of BACE-1 activity in a fluorometric assay

The BACE-1 fluorescence resonance energy transfer (FRET) assay was performed as described by the BACE kit manufacturer (Sigma, product number CS0010)^{67,68} Principle of the assay: The substrate is linked to a fluorescent dye on one end and to a quenching group on its other end. The fluorescence of the substrate is significantly reduced due to intra molecular resonance energy transfer to the quenching group. Upon substrate cleavage by the enzyme, there is a disturbance of the energy transfer resulting in the enhancement of the fluorescent signal. The assay procedure can be described briefly as follows: The BACE substrate is prepared in the buffer to a concentration of 50 μM . BACE enzyme is prepared in the same buffer to a concentration of approximately 0.3 units/ μL . Stock solutions of test samples are prepared in DMSO, and then serially diluted in 50 mM sodium acetate, pH 4.5 to give the desired working concentrations. Triton X-100 was added to each well to a final concentration of 160 μM .

BACE enzyme, substrate, standard, test samples and buffer are then added to the wells for a total volume of 100 μL , with the BACE-1 enzyme being added last, just prior to reading. Baseline fluorescence is recorded immediately after the addition of the BACE enzyme on a fluorometer set at excitation 320 nm, emission 405 nm. The reaction rate was monitored for 2 h at 37 °C using FLX800TBI Microplate Fluorimeter (BioTek Instruments, Winooski, USA) and the linear time-relative fluorescence units (RFU) sections were taken for rate calculation.⁶⁸

4.4. Quantification of renin activity in a fluorometric assay

SensoLyte™ 520 Renin Assay Kit was used for the assay using a Mc-Ala/Dnp FRET peptide. The sequence of this peptide is derived from the cleavage site of renin. In the FRET peptide the fluorescence of Mc-Ala is quenched by Dnp. Upon cleavage into two separate fragments by renin, the fluorescence of Mc-Ala is recovered, and can be monitored at excitation/emission = 490/520 nm.

Test compounds and renin solutions were added into the microplate wells and incubated at 37 °C for 30 min. Subsequently, 50 μL renin substrate solution were added into each well. The reagents were subsequently mixed thoroughly by shaking the plate gently for 30 s. The fluorescence intensity was immediately measured continuously and recorded every 5 min for 15 min at 37 °C. Appropriate positive and negative controls were prepared.⁷³

Acknowledgments

This project was partially sponsored by the Faculty of Graduate Studies (Ph.D. Thesis of Afaf Al-Nadaf). The authors thank the Deanship of Scientific Research and Hamdi-Mango Center for Scientific Research at the University of Jordan for their generous funds. The authors also thank Ms. Hiba Zalloum for her technical assistance.

Supplementary data

Supplementary data associated with this article can be found, in the online version, at doi:10.1016/j.bmc.2010.03.043.

References and notes

- Maria, L. B.; Riccardo, M.; Anna, M.; Michela, R.; Carlo, M. *Curr. Opin. Chem. Biol.* **2009**, *13*, 303.
- Shawn, J. S. *Drug Dev. Res.* **2009**, *70*, 101.
- Jeffrey-Tri, N.; Abdellah, Y.; Yoshiaki, K. *Curr. Pharm. Des.* **2006**, *12*, 4295.
- Li-Bang, Y.; Kristina, L.; Riqiang, Y.; Martin, C.; Weiming, X.; Xiao-Li, Y.; Thomas, B.; Lucia, S.; Philipwong, Donald, P.; Rena, L.; Yong, S. *Nat. Med.* **2003**, *9*.
- Vinicius, B. S.; Adriana, M. N.; Daniela, G. P.; Tainá, F. P.; Carlos, H. T. *Curr. Bioactive Compd.* **2009**, *5*, 119.
- Cooper, J. B. *Curr. Drug Targets* **2002**, *3*, 155.
- Varghese, J. *Curr. Top. Med. Chem.* **2006**, *6*, 569; Schmidt, B.; Baumann, S.; Hannes, A. B.; Larbig, G. *Curr. Top. Med. Chem.* **2006**, *6*, 377.
- Wen-Hai, H.; Rong, S.; Yong-Zhou, H. *Curr. Med. Chem.* **2009**, *16*, 1806.
- Cumming, J. N.; Le, T. X.; Babu, S.; Carroll, X.; Chen, L.; Favreau, P.; Gaspari, T.; Guo, D. W.; Hobbs, Y.; Huang, U.; Iserloh, M. E., et al. *Bioorg. Med. Chem. Lett.* **2008**, *18*, 3236.
- Yoshio, H.; Hiroko, O.; Naoko, M.; Ryoji, Y.; Abdellah, Y.; Koushi, H.; Tooru, K.; Kazuki, S.; Yoshio, H.; Shoichi, I.; Yoshiaki, K. *Bioorg. Med. Chem. Lett.* **2008**, *18*, 1654.
- Lorna, P.; Andrea, C.; Francesco, C.; Federica, B.; Manuela, B.; Francesca, M.; Maurizio, R.; Vincenza, A.; Angela, R. *Bioorg. Med. Chem. Lett.* **2008**, *18*, 423.
- Yoshiari, S.; Takeshi, K.; Akinori, A.; Tetsuhiro, N.; Hachiro, S. *Biochim. Biophys. Acta* **2008**, *1780*, 819.
- Heuisul, P.; Kyeongsik, M.; Hyo-Shin, K.; Ki, D. K.; Dongchul, L.; Sang-Won, S.; Jae-Ung, C.; Bettina, P.; Deog-Young, C. *Bioorg. Med. Chem. Lett.* **2008**, *18*, 2900.
- Derek, C. C.; Joseph, R. S.; Rajiv, C.; Rebecca, C.; John, W. E.; Kristi, Y. F.; Boyd, L. H.; Yun, H.; Steve, J.; Lee, D. J.; Guixian, J.; Peter, A. L.; Michael, S. M.; Eric, S. M.; William, J. M.; Mary-Margaret, O.; Andrea, M. O.; Albert, J. R.; Kristine, S.; JunJun, W.; Eric, W.; Jonathan, B. *Bioorg. Med. Chem. Lett.* **2008**, *18*, 1063.
- Huang, D.; Urs, L.; Peter, K.; Marco, C.; Alcide, B.; Amedeo, C. *J. Am. Chem. Soc.* **2006**, *128*, 5436.
- Arun, K. G.; Geoffrey, B.; Cynthia, H.; Reiko, K.; Dongwoo, S.; Khaja, A.; Lin, H.; Jeffrey, A. L.; Chan, N.; Gerald, K.; Jacques, E.; Jordan, T. *J. Med. Chem.* **2001**, *44*, 2865.
- Godemann, R.; Madden, J.; Kramer, J.; Smith, M. A.; Fritz, U.; Hesterkamp, T.; Barker, J.; Hoepfner, S.; Hallett, D.; Cesura, A.; Ebneith, A.; Kemp, J. *Biochemistry-Us* **2009**, *48*, 10743.
- Charrier, N.; Clarke, B.; Cutler, L.; Demont, E.; Dingwall, C.; Dunsdon, R.; Hawkins, J.; Howes, C.; Hubbard, J.; Hussain, I.; Maile, G.; Matico, R.; Mosley, J.; Naylor, A.; O'Brien, A.; Redshaw, S.; Rowland, P.; Soleil, V.; Smith, K. J.; Sweitzer, S.; Theobald, P.; Vesey, D.; Walter, D. S.; Wayne, G. *Bioorg. Med. Chem. Lett.* **2009**, *19*, 3664.
- Charrier, N.; Clarke, B.; Demont, E.; Dingwall, C.; Dunsdon, R.; Hawkins, J.; Hubbard, J.; Hussain, I.; Maile, G.; Matico, R.; Mosley, J.; Naylor, A.; O'Brien, A.; Redshaw, S.; Rowland, P.; Soleil, V.; Smith, K. J.; Sweitzer, S.; Theobald, P.; Vesey, D.; Walter, D. S.; Wayne, G. *Bioorg. Med. Chem. Lett.* **2009**, *19*, 3669.
- Charrier, N.; Clarke, B.; Cutler, L.; Demont, E.; Dingwall, C.; Dunsdon, R.; Hawkins, J.; Howes, C.; Hubbard, J.; Hussain, I.; Maile, G.; Matico, R.; Mosley, J.; Naylor, A.; O'Brien, A.; Redshaw, S.; Rowland, P.; Soleil, V.; Smith, K. J.; Sweitzer, S.; Theobald, P.; Vesey, D.; Walter, D. S.; Wayne, G. *Bioorg. Med. Chem. Lett.* **2009**, *19*, 3674.
- Clarke, B.; Demont, E.; Dingwall, C.; Dunsdon, R.; Faller, A.; Hawkins, J.; Hussain, I.; Macpherson, D.; Maile, G.; Matico, R.; Milner, P.; Mosley, J.; Naylor, A.; O'Brien, A.; Redshaw, S.; Riddell, D.; Rowland, P.; Soleil, V.; Smith, K.; Stanway, S.; Stemp, G.; Sweitzer, S.; Theobald, P.; Vesey, D.; Walter, D. S.; Ward, J.; Wayne, G. *Bioorg. Med. Chem. Lett.* **2008**, *18*, 1017.
- Beswick, P.; Charrier, N.; Clarke, B.; Demont, E.; Dingwall, C.; Dunsdon, R.; Faller, A.; Gleave, R.; Hawkins, J.; Hussain, I.; Johnson, C. N.; Macpherson, D.; Maile, G.; Matico, R.; Milner, P.; Mosley, J.; Naylor, A.; O'Brien, A.; Redshaw, S.; Riddell, D.; Rowland, P.; Skidmore, J.; Soleil, V.; Smith, K. J.; Stanway, S.; Stemp, G.; Stuart, A.; Sweitzer, S.; Theobald, P.; Vesey, D.; Walter, D. S.; Ward, J.; Wayne, G. *Bioorg. Med. Chem. Lett.* **2008**, *18*, 1022.
- Clarke, B.; Demont, E.; Dingwall, C.; Dunsdon, R.; Faller, A.; Hawkins, J.; Hussain, I.; Macpherson, D.; Maile, G.; Matico, R.; Milner, P.; Mosley, J.; Naylor,

- A.; O'Brien, A.; Redshaw, S.; Riddell, D.; Rowland, P.; Soleil, V.; Smith, K.; Stanway, S.; Stemp, G.; Sweitzer, S.; Theobald, P.; Vesey, D.; Walter, D. S.; Ward, J.; Wayne, G. *Bioorg. Med. Chem. Lett.* **2008**, *18*, 1011.
24. Beeley, N. R. A.; Sage, C. *Targets* **2003**, *2*, 19.
25. Klebe, G. *Drug Discovery Today* **2006**, *11*, 580.
26. Steuber, H.; Zentgraf, M.; Gerlach, C.; Sottriffer, C. A.; Heine, A.; Klebe, G. *J. Mol. Biol.* **2006**, *363*, 174.
27. Stubbs, M. T.; Reyda, S.; Dullweber, F.; Moller, M.; Klebe, G.; Dorsch, D.; Mederski, W.; Wurziger, H. *ChemBioChem* **2002**, *3*, 246.
28. DePristo, M. A.; de Bakker, P. I. W.; Blundell, T. L. *Structure* **2004**, *12*, 831.
29. Georgia, B. M.; Dennis, C.; Samuel, L. G.; Ming-Tain, L.; Sanjeev, K. M.; Philippe, G. N.; Beth, P.; Hemaka, A. R.; Harold, G. S.; Shaun, R. S.; Katharine, M. H. *Bioorg. Med. Chem. Lett.* **2007**, *17*, 1117.
30. Taha, M. O.; Bustanji, Y.; Al-Ghoussein, M.; Mohammad, M.; Zalloum, H.; Al-Masri, I. M.; Atallah, N. *J. Med. Chem.* **2008**, *51*, 2062.
31. Taha, M. O.; Dahabiyeh, L. A.; Bustanji, Y.; Zalloum, H.; Saleh, S. *J. Med. Chem.* **2008**, *51*, 6478.
32. Taha, M. O.; Atallah, N.; Al-Bakri, A. G.; Paradis-Bleau, C.; Zalloum, H.; Younis, K.; Levesque, R. C. *Bioorg. Med. Chem.* **2008**, *16*, 1218.
33. Taha, M. O.; Bustanji, Y.; Al-Bakri, A. G.; Yousef, M.; Zalloum, W. A.; Al-Masri, I. M.; Atallah, N. *J. Mol. Graphics Modell.* **2007**, *25*, 870.
34. Abu Hammad, A. M.; Taha, M. O. *J. Chem. Inf. Model.* **2009**, *49*, 978.
35. *CATALYST 4.11 Users' Manual*; Accelrys Software Inc.: San Diego, CA, 2005.
36. Sprague, P. W.; Hoffmann, R.; Van de Waterbeemd, H.; Testa, B.; Folkers, G. *Curr. Tools Med. Chem.* **1997**, 230.
37. Barnum, D.; Greene, J.; Smellie, A.; Sprague, P. *J. Chem. Inf. Comput. Sci.* **1996**, *36*, 563.
38. Smellie, A.; Teig, S.; Towbin, P. *J. Comput. Chem.* **1995**, *16*, 171.
39. Li, H.; Sutter, J.; Hoffmann, R. In *Pharmacophore Perception, Development, and Use in Drug Design*; Güner, O. F., Ed.; International University Line: La Jolla, CA, 2000; pp 173–189.
40. Sutter, J.; Güner, O.; Hoffmann, R.; Li, H.; Waldman, M. In *Pharmacophore Perception, Development, and Use in Drug Design*; Güner, O. F., Ed.; International University Line: La Jolla, CA, 2000; pp 501–511.
41. Kurogi, Y.; Güner, O. F. *Curr. Med. Chem.* **2001**, *8*, 1035.
42. Bersuker, I. B.; Bahçeci, S.; Boggs, J. E. In *Pharmacophore Perception, Development, and Use in Drug Design*; Güner, O. F., Ed.; International University Line: La Jolla, CA, 2000; pp 457–473.
43. Poptodorov, K.; Luu, T.; Langer, T.; Hoffmann, R. In *Methods and Principles in Medicinal Chemistry. Pharmacophores and Pharmacophores Searches*; Hoffmann, R. D., Ed.; Wiley-VCH: Weinheim, Germany, 2006; 2, pp 17–47.
44. Singh, J.; Chuaqui, C. E.; Boriack-Sjodin, P. A.; Lee, W. C.; Pontz, T.; Corbley, M. J.; Cheung, H. K.; Arduini, R. M.; Mead, J. N.; Newman, M. N.; Papadatos, J. L.; Bowes, S.; Josiah, S.; Ling, L. E. *Bioorg. Med. Chem. Lett.* **2003**, *13*, 4355.
45. Taha, M. O.; Qandil, A. M.; Zaki, D. D.; Aldamen, M. A. *Eur. J. Med. Chem.* **2005**, *40*, 701.
46. Taha, M. O.; Bustanji, Y.; Al-Ghoussein, M. A. S.; Mohammad, M.; Zalloum, H.; Al-Masri, I. M.; Atallah, N. *J. Med. Chem.* **2008**, *51*, 2062.
47. Taha, M. O.; Al-Bakri, A. G.; Zalloum, W. A. *Bioorg. Med. Chem. Lett.* **2006**, *16*, 5902.
48. Garino, C.; Tomita, T.; Pietrancosta, N.; Laras, Y.; Rosas, R.; Herbertte, G.; Maigret, B.; Quéféver, G.; Iwatsubo, T.; Kraus, J. *J. Med. Chem.* **2006**, *49*, 4275.
49. Sheridan, R. P.; Kearsley, S. K. *Drug Discovery Today* **2002**, *7*, 903.
50. Fischer, R. *The Principle of Experimentation Illustrated by a Psycho-Physical ExpeHafner Publishing Co.*, 8th ed.; Hafner Publishing.
51. *CERIUS2, QSAR Users' Manual*, version 4.10; Accelrys Inc.: San Diego, CA, 2005, 43–88, 221–235.
52. Ramsey, L. F.; Schafer, W. D. *The Statistical Sleuth*, 1st ed.; Wadsworth Publishing Company: Belmont, CA, 1997.
53. Kier, L. B.; Hall, L. H. In *Topological Indices and Related Descriptors in QSAR and QSPR*; Devillers, J.; Balaban, A. T., Eds.; Gordon and Breach: London, 1999; pp 491–562.
54. Andrew, L. H.; Colin, R. G.; Alexander, A. *Drug Discovery Today* **2004**, *9*, 430.
55. Kirchmair, J.; Markt, P.; Distinto, S.; Wolber, G.; Langer, T. *J. Comput. Aided Mol. Des.* **2008**, *22*, 213.
56. Verdonk, M. L.; Marcel, L.; Berdini, V.; Hartshorn, M. J.; Mooij, W. T. M.; Murray, C. W.; Taylor, R. D.; Watson, P. *J. Chem. Inf. Comput. Sci.* **2004**, *44*, 793.
57. Irwin, J. J.; Shoichet, B. K. *J. Chem. Inf. Comput. Sci.* **2005**, *45*, 177.
58. Triballeau, N.; Acher, F.; Brabet, I.; Pin, J.-P.; Bertrand, H.-O. *J. Med. Chem.* **2005**, *48*, 2534.
59. Gao, H.; Williams, C.; Labute, P.; Bajorath, J. *J. Chem. Inf. Comput. Sci.* **1999**, *39*, 164.
60. Jacobsson, M.; Liden, P.; Stjernschantz, E.; Bostroem, H.; Norinder, U. *J. Med. Chem.* **2003**, *46*, 5781.
61. Darvesh, S.; McDonald, R. S.; Darvesh, K. V.; Mataija, D.; Mothana, S.; Cook, H.; Carneiro, K. M.; Richard, N.; Walsh, R.; Martin, E. *Bioorg. Med. Chem.* **2006**, *14*, 4586.
62. Shunqi, Y.; Todd, A.; Esmir, G.; Jae Hoon, S.; Tania, T.; Hongwoo, K.; Frank, R.; Huaming, C.; Robert, H.; Wu, J. Z.; Zhi, H.; Nanhua, Y. *Bioorg. Med. Chem. Lett.* **2007**, *17*, 28.
63. Chuansheng, N.; Jun, L.; Terrence, W. D.; Shu-Hui, C. *Tetrahedron* **1998**, *54*, 6311.
64. Brett, D. A.; Victor, K. P.; Laura, C. M.; Mark, R.; Magda, M.; Clodagh Prendergast, ; Terry, B.; Guy, L.; Jamie, F.; Lina, L.; Xiaodong, W.; Hariharan, V.; Marna, P.; Craig, W.; Michele, C. R.; Michael, H.; Kenway, H.; Xiaohu, D.; Christopher, K.; Nigel, P. S.; Michael, H. R. *J. Med. Chem.* **2006**, *49*, 6371.
65. Laixing, H.; Zhuo-rong, L.; Yan, L.; Jinrong, Q.; Yi-He, L.; Jian-dong, J.; David, W. B. *J. Med. Chem.* **2006**, *49*, 6273.
66. Sante, M.; Maria, D.; Barbara, S.; Maria, B.; Edward, B. *J. Med. Chem.* **1988**, *31*, 1956.
67. BACE1 Activity Detection Kit (Fluorescent), CS0010.
68. Francesca, M.; Marina, N.; Vanni, C.; Vincenza, A. *Anal. Bioanal. Chem.* **2007**, *388*, 1175.
69. *CERIUS2 4.10 LigandFit User Manual*; Accelrys Inc.: San Diego, CA, 2000; Venkatachalam, C. M.; Jiang, X.; Oldfield, T.; Waldman, M. *J. Mol. Graphics Modell.* **2003**, *21*, 289.
70. Perioli, L.; Ambrogio, V.; Bernardini, C.; Grandolini, G.; Ricci, M.; Giovagnoli, S.; Rossi, C. *Eur. J. Med. Chem.* **2004**, *39*, 715.
71. Laszlo, P.; Katalin, P.; Alevtina, D. Z.; Vien, N.; Pal, P.; Stanley, M. S. *J. Med. Chem.* **2004**, *47*, 6025.
72. Huang, W.; Yu, H.; Sheng, R.; Li, J.; Hu, Y. *Bioorg. Med. Chem.* **2008**, *16*, 10190.
73. Sensolyte™ 390 Renin Assay Kit.
74. Cronin, M. T. D.; Schultz, T. W. *J. Mol. Struct. (Theochem.)* **2003**, *622*, 39.
75. Sinha, S.; Anderson, J. P.; Barbour, R.; Basi, G. S.; Caccavello, R.; Davis, D.; Doan, M.; Dovey, H. F.; Frigon, N.; Hong, J.; Jacobson-Croak, K.; Jewett, N.; Keim, P.; Knops, J.; Lieberburg, I.; Power, M.; Tan, H.; Tatsuno, G.; Tung, J.; Schenk, D.; Seubert, P.; Suomensari, S. M.; Wang, S.; Walker, D.; Zhao, J.; McConlogue, L.; John, V. *Nature* **1999**, *402*, 537.
76. Taha, M. O.; Tarairah, M.; Zalloum, H.; Abu-Sheikha, G. *J. Mol. Graphics Modell.* **2010**, *28*, 383.
77. Rajapakse, H. A.; Nantermet, P. G.; Selnick, H. G.; Munshi, S.; Mcgaughey, G. B.; Lindsley, S. R.; Young, M. B.; Laia, M. T.; Espeseth, S.; Shi, X. P.; Colussi, D.; Pietrakm, B.; Crouthamel, C.; Tugusheva, K.; Huang, Q.; Xu, M.; Simon, A. J.; Kuo, L.; Hazuda, D. J.; Graham, S.; Vacca, J. P. *J. Med. Chem.* **2006**, *49*, 7270.